Robertson Wesley Monteiro Pires Junior

Development of multifunctional structures for measuring temperature, strain, angle, and vibration frequencies using additive manufacturing techniques

Vitória, Brazil

2024

Robertson Wesley Monteiro Pires Junior

Development of multifunctional structures for measuring temperature, strain, angle, and vibration frequencies using additive manufacturing techniques

Master Dissertation submitted to the Electrical Engineering Postgraduate Program of the Technological Center of the Federal University of Espírito Santo, as partial requirement for obtaining a Master Degree in Electrical Engineering.

Federal University of Espírito Santo

Electrical Engineering Postgraduate Program

Supervisor Prof. Dr. Arnaldo Gomes Leal Junior

Co-supervisor: Prof. Dr. Anselmo Frizera Neto

Vitória, Brazil

2024

Ficha catalográfica disponibilizada pelo Sistema Integrado de
Bibliotecas - SIBI/UFES e elaborada pelo autor

Pires Junior, Robertson Wesley Monteiro, 1992-
P667d Development of multifunctional structures for measuring temperature, strain, angle, and vibration frequencies using additive manufacturing techniques / Robertson Wesley Monteiro Pires Junior. - 2024.
67 f. : il.

Orientador: Arnaldo Gomes Leal Junior.
Coorientador: Anselmo Frizera Neto.
Dissertação (Mestrado em Engenharia Elétrica) - Universidade Federal do Espírito Santo, Centro Tecnológico.

1. Optical fibers. 2. Sensors. I. Leal Junior, Arnaldo Gomes. II. Frizera Neto, Anselmo. III. Universidade Federal do Espírito Santo. Centro Tecnológico. IV. Título.

CDU: 621.3

Robertson Wesley Monteiro Pires Junior

Development of multifunctional structures for measuring temperature, strain, angle, and vibration frequencies using additive manufacturing techniques

Master Dissertation submitted to the Electrical Engineering Postgraduate Program of the Technological Center of the Federal University of Espírito Santo, as partial requirement for obtaining a Master Degree in Electrical Engineering.

Approved on April 17th, 2024.

Arnaldo Gomes Leal Junior

Prof. Dr. Arnaldo Gomes Leal Junior
Federal University of Espírito Santo
Supervisor

Anselmo Frizera Neto

Prof. Dr. Anselmo Frizera Neto
Federal University of Espírito Santo
Co-supervisor

Documento assinado digitalmente
gov.br
CAMILO ARTURO RODRIGUEZ DIAZ
Data: 17/07/2024 08:10:47-0300
Verifique em https://validar.iti.gov.br

Prof. Dr. Camilo Arturo Rodriguez Diaz
Federal University of Espírito Santo
Examiner

Assinado por: CARLOS ALBERTO FERREIRA MARQUES -
Num. de Identificação: BI12526793
Data: 2024.07.17 09.36.38 GMT Daylight time
CHAVE MÓVEL

Prof. Dr. Carlos A. F. Marques
University of Aveiro
Examiner

Vitória, Brazil
2024

Statement of Authorship

I hereby declare that the thesis submitted is my own work. All direct or indirect sources used are acknowledged as references. I further declare that I have not submitted this thesis at any other institution in order to obtain a degree.

Acknowledgments

I owe immense gratitude to God, as He came to my aid in times of doubt and distress. Just as I owe thanks to my family, to my mother Andeia Neves Cardoso Pires, and my father Robertson Wesley Monteiro Pires, for being my safe haven and ensuring that I could complete the work in my own time. Furthermore, I would like to express my gratitude to Natalia Ferreira Paiva, my life companion, who always supports me and believes in my abilities.

There are also those who taught me everything I needed to successfully develop my work, my advisor Prof. Dr. Arnaldo Gomes Leal Junior, and my co-advisor Prof. Dr. Anselmo Frizera Neto, who are part of the PPGEE UFES. Additionally, I would like to thank my colleagues from LabSensores for the friendly atmosphere, and especially Leandro Macedo Cassa for his assistance in some experiments.

Finally, the work would not have been possible without the financial support from funding sources including CNPq (310709/2021-0, 403753/2021-0, 405336/2022-5, and 440064/2022-8), FAPES (1004/2022 and 2022-C5K3H), and MCTI/FNDCT/FINEP (2784/20 and 0036/21) projects.

Abstract

This Master Dissertation presented the development of different multifunctional structures embedded with fiber Bragg gratings (FBGs). Additive manufacturing techniques were used to manufacture these structures. The manufactured multifunctional structures consist of an artificial tendon capable of monitoring deformation parameters, temperature, and curvature angle; a temperature sensor capable of measuring it in different environments; and a frequency meter in the form of a cantilever beam. The artificial tendon was manufactured by pouring polyurethane resin (PU) into a mold made with polylactic acid (PLA) filament so that the resin coated the FBGs. The temperature sensor was manufactured with light-cured resin and the FBG was embedded in an aperture in the structure. Two accelerometers were manufactured by FFF using filaments of nylon and 17-4 PH, which is stainless steel but in the form of a filament aggregated with polymeric particles. The materials used to manufacture the structures were characterized by static and dynamic mechanical tests. In static tests, it was noted that Young's modulus (E) increases as a function of the increase in the cross-section of the specimen, which was modified by varying the infill and wall thickness of the body. However, the mechanical resistance of the optical fiber predominated over these constructive characteristics after embedding in the test specimens. This impact is more noticeable in the results of the fiber embedded in PU since the test specimen's E with the fiber embedded is almost 10 times greater than that with raw PU. In dynamic tests, the amorphous polymer chains of nylon embedded with fiber cause the material to present different E during its transition to the rubbery plateau, which is only reached from 60 °C, while 17-4 PH shows no difference notable in E when the vibration frequency varies. The artificial tendon was characterized for strain showing different sensitivities between the FBGs positioned in the center and close to the tendon wall. Furthermore, the tendon presented an average sensitivity of 9.06 pm/°C for characterization between 0 °C and 30 °C and a root mean square error of 3.25 ° when the curvature angle varied from 0° to 90°. The 17-4 PH accelerometer cantilever showed sensitivity of 1.79 pm/V in the range from 0.5 V to 2.0 V when the shaker was set to 10 Hz and 3.61 pm/V for 100 Hz. Therefore, in future works, the intention is to apply the multifunctional structures developed, with the artificial tendon being used in the actuation of robotic parts, and the accelerometers in predictive vibration analysis, for example.

Keywords: Multifunctional structures, Sensors, Additive manufacturing

Resumo

Essa Dissertação de Mestrado apresentou o desenvolvimento de diferentes estruturas multifuncionais embutidas com redes de Bragg em fibras ópticas (FBGs). Para a fabricação dessas estruturas foram utilizadas técnicas de manufatura aditiva, por ser um método de fabricação que se popularizou principalmente a partir do advento das impressoras de fabricação por filamento fundido (FFF). As estruturas multifuncionais fabricadas consistem em um tendão artificial capaz de monitorar parâmetros de deformação, temperatura e ângulo de curvatura; um sensor de temperatura capaz de medi-la em diferentes ambientes; e um medidor de frequência na forma de uma viga em balanço. O tendão artificial foi fabricado ao escoar a resina de poliuretano (PU) dentro de um molde fabricado com filamento de poliácido láctico (PLA), de forma que a resina resvestisse as FBGs. O sensor de temperatura foi fabricado com resina fotopolimerizável e a FBG foi embutida em um orifício na estrutura. Foram fabricados dois acelerômetros por FFF utilizando filamentos de náilon e 17-4 PH, que é um aço inoxidável mas na forma de filamento está agregado com particulados poliméricos. Os materiais utilizados na fabricação das estruturas foram caracterizados por ensaios mecânicos estáticos e dinâmicos. Nos ensaios estáticos notou-se que o módulo de Young (E) aumenta em função do aumento da seção transversal do corpo de prova, que foi modificada através da variação do preenchimento e da espessura de parede do corpo. Contudo, a resistência mecânica da fibra óptica predominou sobre essas características construtivas após o seu embutimento nos corpos de prova. Esse impacto fica mais perceptível nos resultados da fibra embutida no PU, já que o E do corpo de prova com a fibra embutida é quase 10 vezes maior do que com o PU bruto. Nos ensaios dinâmicos as cadeias poliméricas amorfas do náilon embutido com fibra fazem com o material apresente diferentes E durante sua transição até o platô de borracha, que só é atingido a partir de 60 °C, enquanto o 17-4 PH não apresenta diferença notável em E quando a frequência de vibração varia. O tendão artificial foi caracterizado para strain apresentando diferentes sensibilidades entre as FBGs posicionadas no centro e próximas da parede do tendão. Além disso, o tendão apresentou sensibilidade média de 9.06 pm/°C para caracterização entre 0°C e 30°C e uma raiz do erro quadrático médio de 3.25º quando o ângulo de curvatura variou de 0º até 90º. O sensor de temperatura teve a sensibilidade diminuida, sendo necessário utilizar um novo projeto para esta estrutura. Por fim, o cantilever de aquisição de frequência de 17-4 PH mostrou sensibilidade para a variação de amplitude de vibração (que variou de 0.5 V até 2.0 V) de 1.79 pm/V quando vibrado na frequência de 10 Hz e 3.61 pm/V para 100 Hz. Portanto, em trabalhos futuros, pretende-se aplicar as estruturas multifuncionais desenvolvidas, com o tendão artificial sendo utilizado no acionamento de peças robóticas, e os acelerômetros na análise preditiva de vibrações, por exemplo.

Keywords: Estruturas multifuncionais, Sensores, Manufatura aditiva

Contents

List of Figures

List of Tables

List of Acronyms

AM	Additive Manufacturing
ASTM	American Society for Testing and Materials
BJ	Binder Jetting
DED	Directed Energy Deposition
DOD	Drop-On-Demand
FBG	Fiber Bragg Grating
FFF	Fused Filament Fabrication
FFT	Fast Fourier Transform
fs-IR	Femtosecond Infrared
IoT	Internet of Things
LED	Light-Emitting Diode
MEX	Material Extrusion
MJ	Material Jetting
OFS	Optical Fiber Sensor
PBF	Powder Bed Fusion
PLA	Poly Lactic Acid
PU	Polyurethane
SLA	Stereolithography Apparatus
SMF	Single-mode Optical Fiber
TE	Transverse Electric
TM	Transverse Magnetic
TRL	Technology Readiness Level
UV	Ultra Violet
VPP	Vat Photopolymerization
WDM	Wavelength Division Multiplexing

List of Symbols

$\mathtt{E}$	Electric field intensity
β	Propagation constant
ω	Wave frequency
t	Time
ϕ	Phase angle
v	Wave velocity
n	Medium refractive index
μ	Medium permittivity
ξ	Medium permeability
K	Wave vector
λ	Wavelength in vacuum
κ	Transverse propagation constant
γ	Decay constant
r	Fiber core radius
θ	Angle between the propagating wave and the perpendicular line to the core-cladding interface
λ_B	Bragg wavelength
n_eff	Effective refractive index
Λ	Grating periodicity
Λ_{pm}	Phase mask grating periodicity
Δ	Variation
P_e	Pockel's coefficient
ε_z	Z-direction strain
α	Thermal expansion coefficient

ψ	Thermo-optic coefficient
T	Temperature
∂	Partial derivative
ξ	Deformation
F	Force
L	Length
E	Young’s Modulus
I	Moment of inertia
ε	Deformation
k	Stiffness
A	Wave amplitude
ω_n	System’s natural frequency
m, M	Mass
σ	Stress
ε	Strain
E*	Complex Young’s Modulus
E’	Elastic Young’s Modulus
E”	Imaginary Young’s Modulus
δ	Phase angle between E’ and E*
v_f	Free volume
T_γ	Gamma transition temperature
T_β	Beta transition temperature
T_g	Glass transition temperature
T_m	Melt transition temperature
M_e	Molecular weight between entanglements

1 Introduction

1.1 Motivation

The advance and wide adoption of various sensor systems that can be integrated into different structures have been the driving force behind the development of multifunctional structures [1]. These structures are termed multifunctional for their ability to serve multiple functions within their application and combine structural support with sensor functionality [1]. By integrating sensors into these structures, they not only contribute to the structural integrity of a system but also gather data, serving dual roles. Furthermore, with the increasing demand for smart devices and structures, inside the particular context of the Internet of Things (IoT) [2], there has been a surge in the development of flexible sensor systems capable of embedding into complex structures [3]. As a result, the efforts invested in the development of multifunctional structures have found significant applications in diverse fields such as structural health monitoring [4], robotics [5], industrial process monitoring [6], and biomechanical applications [7]. In addition, for biomechanics, bioengineering advancements, and biomimetic devices, where the use of assistive tools is utilized, the integration of multifunctional structures has played a pivotal role in driving innovation and addressing complex challenges.

An integral aspect of multifunctional structure development lies in sensor integration, offering the capability to sense various parameters in both the environment and the structure itself. In this regard, optical fiber sensors (OFSs) stand out due to their small dimensions and lightweight nature, making them well suited for integration into structures [8]. Moreover, a biomimetic approach has emerged as a key area of study, aimed at developing embedded sensors using multifunctional materials [9]. Among the various geometries and functionalities found in nature, there is particular interest in the study and development of artificial tendons [10]. Tendons play a crucial role in withstanding traction, however they are susceptible to partial or complete rupture. As a solution, artificial prosthetic tendons made of biocompatible materials can be used to replace damaged tendons. Furthermore, artificial tendons are utilized in orthoses for rehabilitating individuals affected by stroke, helping the mobility recovery of affected limbs [11], [12].

Multifunctional structures can also have important applications in healthcare through integrated assistive devices and clothing-integrated wearable sensors [5], [13]. This approach seeks to develop wearable devices based on flexible sensors, which enhance the interaction between humans and robots by increasing compliance. Drawing inspiration from the biological forms and structures found in nature, these multifunctional structures can mimic natural shapes using flexible materials [14]. Moreover, the focus on flexible materials and bioinspired shapes reflects an approach aimed at creating user-friendly devices that adapt to the natural movements and physiology of the human body. This emphasis on flexibility and bioinspiration not only improves comfort but also ensures seamless integration into daily life, promoting the widespread adoption of wearable healthcare technologies [15].

Among the sensors that can be integrated into a multifunctional structure, OFSs present intrinsic advantages that are suitable for integration into multifunctional structures [16]. Their lightweight and compact nature ensure minimal impact on the overall weight and size of the structure, making them suitable for integration [17]. Additionally, OFSs exhibit excellent chemical stability, allowing them to withstand harsh environmental conditions without degradation [18]. Their immunity to electromagnetic fields ensures accurate and reliable measurements in electrically noisy environments [19]. Furthermore, OFSs possess multiplexing capabilities, enabling multiple sensors to share the same optical fiber, thus reducing complexity and cost [20]. Overall, these advantages make OFS suitable for integration into multifunctional structures.

1.2 Objectives

The main objective of this Master's Thesis is the development of multifunctional structures using additive manufacturing (AM) to manufacture polymeric structures that can be embedded with OFS. These manufactured structures will be used to detect different parameters and will be subjected to different characterizations. To this end, a structure for measuring temperature in variable environment conditions, an artificial tendon, and a cantilever accelerometer will be produced, all embedded with fiber Bragg gratings (FBGs). The artificial tendon will be subjected to measurements of strain, temperature, and curvature. Throughout this work, the following specific objectives were fulfilled:

1. Study the variation of infill parameters, as well as layer and wall thicknesses on the influence of the mechanical resistance of a structure manufactured with AM;
2. Analyze the influence of optical fiber embedding on the mechanical resistance of a structure in static and dynamic tests;
3. Fabrication and characterization of multifunctional structures (artificial tendon, versatile environmental temperature sensor, and cantilever accelerometer) with embedded FBG sensors.

1.3 Justification

Conventionally, sensor systems use electronic or electromechanical sensors, which can present some drawbacks such as sensitivity to misalignments, sensitivity to electromagnetic fields (undesired when electric actuators are activated in wearable robots), lower compactness, the necessity of frequent calibration, and, in some cases, hysteresis and drift in the sensor response

[21]. Furthermore, the rigidity of these sensors can interfere with the mobility and flexibility necessary for daily use. For these reasons, flexible and lightweight sensors, such as OFS, are recommended for wearable structure applications as they can offer comfort, conformity to the body, and reliable performance during extended use [22].

Biocompatibility refers to the ability of a material to interact favorably with biological systems without causing adverse effects, such as negative immune responses or rejection [23]. Consequently, in AM various biocompatible materials are employed for the production of medical devices, implants, and anatomical models [24]. Among the most common materials used are polyethylene glycol (PEG) [25], poly(lactic acid) (PLA) [26], polyurethanes (PU) [27], high-density polyethylene (HDPE)[28], and biopolymers such as polycaprolactone (PCL) [29]. These materials are selected due to their mechanical, biological and degradable properties, which make them ideal for medical and biocompatible applications [30]. In addition to the diversity offered in materials, AM allows the manufacture of personalized models, leaving the user free to produce any type of structure [31]. This enables the creation of multifunctional structures, in addition to enabling their integration with different sensors, providing the detection of more than one type of parameter, if necessary, which is influenced by the geometry of the structure [32]. When a sensor system monitors more than one type of parameter simultaneously, this system is known as multiparametric, and it is essential in applications ranging from structural health monitoring [33] to medical analyses [34]. Specifically, among the physical, mechanical and dynamic parameters that can be measured by OFS are strain, stress, pressure, vibration frequency, and temperature [35]. These measurements can be performed using a single fiber; therefore, OFS becomes attractive for integration into multiparametric systems.

Considering the advantages of optical fiber integration in different structures, there is a multitude of OFS approaches conventionally employed and proposed in the literature [36]. Among these different approaches, FBG sensors are one of the most commonly used [35]. This widespread use is attributed to the advantages of easy fabrication and signal processing, along with direct multiplexing capability through wavelength division [35]. The integration of FBGs into structures can be observed in works such as [37], [38], where parameters such as pressure, temperature, strain, humidity, and pH are monitored. Furthermore, in works such as [39], FBG sensors are integrated into AM-manufactured structures to monitor strain and temperature. However, to the best of our knowledge, FBG sensors were not incorporated into biomimetic structures such as artificial tendons. The tendons produced use OFS intensity variation to measure stress and strain, as seen in [40]. In addition, it is proposed to manufacture cantilever beams to measure turning frequencies, with the aim of studying the feasibility of AM techniques in manufacturing this type of sensor integrated into structures. Although there are works on vibration transducers using FBGs [41], [42], they do not employ AM and are not intended to produce multifunctional structures. Based on the motivation and justification presented, the use of FBG sensors and their integration into AM-fabricated structures has been proposed in this work.

1.4 Contributions and Publications

This Dissertation presents as contributions the development of multifunctional structures that are light, compact, and easy to replicate, among which is the artificial tendon manufactured from flexible materials and presenting biomimicry; in addition, it can be applied in wearable sensors or orthoses for monitoring temperature, strain, and curvature parameters. Moreover, two more structures were developed, a temperature sensor embedded in resin to isolate possible measurement errors due to environmental action, and the other based on a cantilever beam to be sensitive to mechanical vibrations.

Publications resulting directly from these contributions are listed below.

1. **Article** - Pires-Junior, R., Frizera, A., Marques, C., & Leal-Junior, A. (2023). Development of Fiber-Bragg-Grating-Integrated Artificial Embedded Tendon for Multifunctional Assessment of Temperature, Strain, and Curvature. Sensors, 23(17), 7332.
2. **Article** - PIRES-JUNIOR, Robertson; FRIZERA, Anselmo; LEAL-JUNIOR, Arnaldo. Design of an optical fiber embedded smart artificial tendon for deformation monitoring. Optical Fiber Technology, v. 80, p. 103464, 2023.

Publications not related directly to these contributions are listed below.

1. **Article** - PIRES-JUNIOR, Robertson et al. Three-Dimensional-Printed Fabrication of POFs Using Different Filaments and Their Characterization for Sensing Applications. Polymers, v. 15, n. 3, p. 640, 2023.
2. **Article** - MACEDO, Leandro et al. An alternative to discarded plastic: A report of polymer optical fiber made from recycled materials for the development of biosensors. Optical Fiber Technology, v. 72, p. 103001, 2022.
3. **Article** - PIRES-JUNIOR, Robertson; LEAL-JUNIOR, Arnaldo. Ensemble learning application in multiplexed optical fibser sensor system for liquid level assessment. Measurement, v. 211, p. 112628, 2023.
4. **Article** - LEAL-JUNIOR, Arnaldo et al. Influence of UV Radiation on Mechanical Properties of Polymer Optical Fibers. Polymers, v. 14, n. 21, p. 4496, 2022.

1.5 Dissertation Structure

This Master's Dissertation is divided into five chapters. In Chapter 1, the introduction was made, addressing justifications, objectives, and motivations for the production of multifunctional structures and the possibilities for their implementation to detect physical, chemical, or biological parameters present in industrial, medical, or structural processes, which will require monitoring and control. Chapter 2 presents the theoretical framework of this work, divided into Section 2.1 in which AM techniques and some of their applications are addressed. In addition, in this section, some parameters of the technique used to manufacture multifunctional structures are explained. In Section 2.2, optical fibers are discussed with an explanation of their waveguide characteristics. Due to their intrinsic advantages, optical fibers are the sensing elements embedded in multifunctional structures. In Section 2.3, OFS are discussed, with FBG sensors being the object of interest. This section presents an inscription method for FBGs in optical fibers, the types of FBG that can be produced, the different structures of FBG that can be manufactured, and how FBGs can be used to measure the parameters of interest in this work. At the end of Chapter 2, in Section 2.4, the dynamic and static characterizations of the materials used in multifunctional structures are addressed. In Chapter 3, the test methodologies adopted for the characterization of test specimens manufactured with AM are described, in which the influence of printing parameters will be verified. Furthermore, characterization tests of FBG sensors embedded in the multifunctional structures are presented. Chapter 4 presents the results of the mechanical tests of the materials and the characterizations of the multifunctional structures. This chapter also includes a discussion of the results obtained. In Chapter 5, the work is concluded by addressing the main points about the manufacture and application of multifunctional structures and the main contributions, ending with what can be done in future work.

2 Fundamentals and Theoretical Background

2.1 Additive manufacturing and applications

A manufacturing process in which a part is manufactured by adding material layer by layer is called additive manufacturing (AM) [31], [43]. This part is designed using 3D modeling software to generate a *.stl* document which goes to a second software known as slicer, where in it is possible to predetermine the manufacturing parameters of the design. The main advantage of using AM is the freedom it offers in manufacturing complex and customizable designs, and it is a manufacturing process that has low material waste [31]. In this context, it is possible to find different AM techniques, each one has a unique way of synthesizing the material used in manufacturing, as well as different forms of layer construction, besides the material used in each technique can vary in state (filament, liquid resin, sheet or powder) [43]. AM techniques will be presented in Subsection 2.1.1, including those applied to manufacture multifunctional structures that will be presented later.

In the same way that AM provides the user with the freedom to produce a variety of structures, it will present limitations regarding appearance, quality, and mechanical resistance that will be limited both by the chosen technique and by the parameters used in manufacturing the structure. Therefore, each technique follows a guideline that distinguishes between the characteristics of each one, since the operating principles of the technique affect the project [43]. In this work, two techniques were used to manufacture the multifunctional structures. A derivative of Vat Photopolymerization technique was applied because it utilizes resin as input material and has high resolution between layers if compared with the other used technique, that is Material Extrusion, which became popular mainly due to the affordable price of consumables and printers of fused filament fabrication [44]. Hence, details about the characteristic limitations of the Material Extrusion technique addressed in this work will be addressed in Subsection 2.1.2.

2.1.1 Additive manufacutring techniques

In the literature, it is possible to find AM techniques being addressed using classifications based on the basic technology (or manufacturing principle) or according to the raw material used [43]. In this work, the techniques are presented according to the American Society for Testing and Materials (ASTM) 52900-2017 [45], which classifies them according to the manufacturing principle. Figure 1 shows a diagram with the techniques and their respective derivatives that are mentioned in the following subsections.

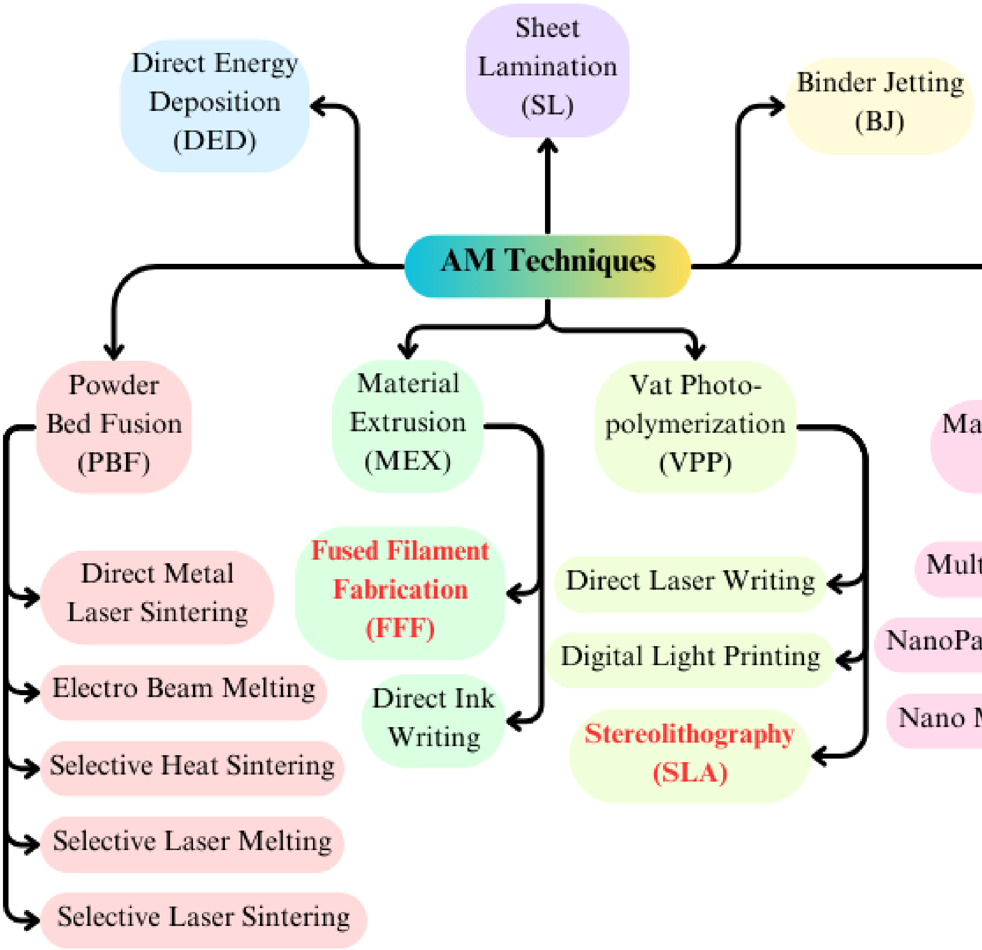

Figure 1 – Additive manufacturing techniques cited in this work. The techniques used in this work are highlighted in red. With FFF, specimens for stress-strain tests, molds for the tendon, and accelerometers were produced. SLA was employed in the fabrication of the temperature sensor structure.

2.1.1.1 Vat Photopolymerization

Vat Photopolymerization (VPP) is the technique that uses a light source to induce the curing of the raw material that is in a liquid state inside a tank [44]. During the cure, the photopolymer monomers are converted into large molecules to construct solid structures [46]. The raw materials developed for VPP include sintering ceramics, elastomers, and resins (which have characteristics like structural, tough, durable, flexible, elastic, castable, biocompatible, and bioink). Over time, the development of sources that emit electromagnetic beams enabled the emergence of VPP derivatives, wherein each one employs a different type of light source ranging from laser beam, solid-state laser, projector, or UV Light-Emitting Diode (LED) [44].

VPP has several derivatives, some of those presented are based on [44]. Direct Laser Writing is used in the microfabrication of microelectronics, tissue engineering, and regenerative medicine. Digital Light Printing is used by jewelry industries, being able to print castable parts. Lithography-based Ceramic can develop components for medical X-ray imaging systems. At last, Stereolithography (SLA) that popularized due to low-cost printers available on the market, finding applications in the dental, manufacturing, art and model, medical, automotive, consumer, and jewelry industries [44]. Also, the file format developed and used for SLA known as Standard Tessellation Language (STL), is being used in almost all AM techniques to transfer the 3D Computer Aided Design model data to a printable file format [44].

2.1.1.2 Powder Bed Fusion

Powder Bed Fusion (PBF) is the technique that fuses material to create layers using high-density energy emission in the form of a laser or electron beam over selected areas, where the emitted energy melts the raw material that is inside a tank [46]. The raw material used in this technique must be in powder form, wherein with the electrons beam is possible to process only metals, while with the laser, beyond metal, the process is achievable in polymers, ceramics, and elastomers [44]. In addition, there are several known derivatives of PBF, including Direct Metal Laser Sintering, Electron Beam Melting, Selective Heat Sintering, Selective Laser Melting (SLM), and Selective Laser Sintering [44].

Laser PBF methods allow the industrial manufacturing of functional parts and tools with complex shapes from metals and ceramic powders [47]. The parts surfaces have excellent to moderate finish, good functional properties, and can be micro- and nanostructured. In addition, the products are usually made from one material, which enables high recyclability of the powder [47]. SLM, for example, enables the production of parts with high technology readiness levels (TLRs are covered briefly in Appendix A) for aerospace (TLRs 5–7), tooling (TLR 9), automotive (TLRs 4–5), and medical industries (TLRs 9–10) [47]. While electron beam PBF is generally limited only to electrically conductive powders, it defines the quite limited selection of materials available for industrial manufacturing [47].

2.1.1.3 Directed Energy Deposition

The Directed Energy Deposition (DED) technique uses a focused energy source (plasma arc, laser beam, and electron beam) to fuse the material, melting it while being deposited onto a substrate, where it solidifies [44]. In this technique, two nozzles are used, one emits the energy for the fusion, the other is responsible for providing material for deposition [44]. There are four types of processes in DED. Two of them use a laser source to melt the material, with their difference lying in the feedstock, which can be either a filament or a powder [48]. Additionally, the other two processes also use filament feedstock, but their energy sources are differentiated as electron beam and electrode [48]. In summary, these processes are classified based on both the energy source and the feedstock type.

The applications of DED include the repair of large, high-value metal parts and even adding material during repair to minimize future erosion or damage in structures [48]. The DED process is also applied in alloy design and multi-material structures. This approach involves the deposition of different alloys to generate composites in specific parts of the structure, resulting in site-specific properties [48]. In addition, DED parts typically require post-processing, such as heat treatment, mechanical treatment, and machining, to achieve the desired shape and mechanical properties.

2.1.1.4 Material Jetting

The Material Jetting (MJ) technique disperses a photopolymer-based resin in the form of liquid droplets from the printing head on the desired substrate and then these droplets are cured using UV light [46]. This technique is highly favorable for the manufacturing of soft objects like soft microrobots and micro absorbers and four-dimensional printed objects, although MJ produces parts with less geometric complexity if compared with other AM techniques [46]. In MJ the liquid exits from the printing heads usually have two modes, the continuous stream mode and the drop-on-demand (DOD) mode, from which the droplets form only with the pressure pulses at specific times using piezoelectric, electrostatic, thermal, or other actuators [46].

The MJ can be used to build parts in wax, metal, and ceramic. The applications include creating master molds and patterns for investment casting that have been adopted by the jewelry industry and expanded to the dental industry that also embraced the technology [44]. The DOD MJ is used to print optical lenses, which by integration of tools in the printing process allows the production of 3D-printed ophthalmic lenses [44]. The derivative MultiJet Printing, also known as MultiJet Modeling or ThermoJet Solid Object Printing, developed the deposition of multi-material printing ranging from polymers, elastomers, multi-material composites, and wax [44]. Some MJ derivatives (NanoParticle Jetting and Nano Metal Jetting) use nano particles of ceramic and metal, the nano-ceramic creates green parts that have enhanced surface finish, while nano-metal ink can make dense metal parts with a high level of surface quality [44].

2.1.1.5 Binder Jetting

The Binder Jetting (BJ) technique uses powder material deposition followed by printing binder agents selectively onto the powder bed in layers forming a green part, then it is sent for further post-processing to obtain the final part [44]. Unlike MJ, the BJ technique does not require a laser, it makes the printing process cheaper and faster than MJ [46]. In the BJ technique, a significant input parameter is related to binder saturation, which is an estimation of powder bed density, and influences the quality (i.e., surface quality and geometric accuracy) of manufactured parts [46].

The BJ applications include tooling and prototyping, producing casting molds for the metal-casting industry, investment casting molds and cores, direct and indirect printing technologies for metal, ceramic, sands, and composite materials dedicated to mainly tooling and dental industries, electronic and pharmaceutical, and finally, produce precision metals parts [44].

2.1.1.6 Sheet Lamination

In the Sheet Lamination (SL) technique, the material is deposited in a sheet form and the process is followed by the shaping operation, which includes stacking, bonding and cutting [46]. The first commercial SL derivative is Laminated Object Manufacturing using paper-based materials and a CO_2 laser cutter [44]. To date, a wide range of materials, including paper, polymer, ceramic, metal, and composite materials, can be manufactured through the SL system, where ultrasonic welding, thermal bonding, adhesive bonding, and clamping are commonly used methods [44]. Other derivatives of SL can make high-quality parts suitable for use in aerospace, automotive, consumer products, sporting goods, and medical use [44].

2.1.1.7 Material Extrusion

In the Material Extrusion (MEX) technique, the material is pushed out through a nozzle and deposited on a platform [44]. In this technique, the nozzle has two degrees of freedom (X and Y) to manufacture each cross-section of the part, while the third degree of freedom (Z) advances the nozzle to the next layer [49]. Furthermore, it is possible to use more than one nozzle in a print, allowing for the manufacture of parts composed of multiple materials [49]. A significant factor for manufacturing using the MEX technique is the exit diameter of the extrusion nozzle because it determines the minimum feature size and printing resolution [49].

MEX has two known derivatives: the first is the fused filament fabrication (FFF) process, in which the extruded material is necessarily a filament; and the second is the continuous direct ink writing (DIW) process, in which a liquid or semi-liquid that is consistent and continuous is extruded to manufacture the part [49]. These aforementioned derivatives are shown in Figure 2. In contrast to the FFF process which is mainly adopted in macro- and meso-scale manufacturing applications, the continuous DIW process is mainly utilized in meso- and micro-scales [49].

The filaments used in the FFF process are typically thermoplastic materials, with the most common being acrylonitrile butadiene styrene (ABS), polylactic acid (PLA), polyether ether ketone (PEEK), polycarbonate (PC), and nylon (or polyamide) [44]. These materials are chosen for their ability to be molded and quickly solidify upon cooling. Additionally, the mechanical, physical, electrical, and magnetic properties of these thermoplastics can be enhanced by incorporating additives, such as metallic powders, glassy fillers, and carbon-based nanomaterials, to form composite filaments of polymer and fiber reinforcement [49].

DIW has available solutions based on polymers, ceramics, metals, alloys, hydrogels, waxes, nanoparticles, or combinations thereof [49]. These solutions are commonly referred to as inks. Their shear strain significantly contributes to the extrusion flow and the extrudability from the extruder [49]. Furthermore, inks should possess a self-healing rheological property, which is described as the capability to recover their mechanical properties once the shear strain is removed [49].

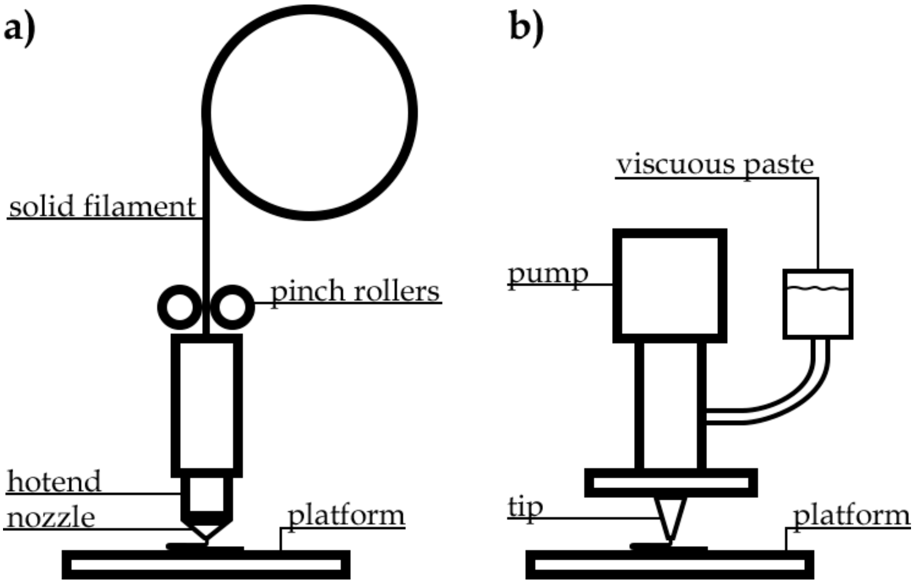

Figure 2 – Schematic of the material extrusion process. **(a)** represents fused filament fabrication and **(b)** direct ink writing. Adapted from [49].

MEX is generally inexpensive, easy to operate, and requires minimal maintenance [49]. The materials used in the FFF process are relatively abundant in the market and available in different variants [49]. In addition, MEX has made significant contributions to the field of healthcare, ranging from the fabrication of customized implants to dental prototypes, scaffolds, and even living organs [50]. Another emerging application is in the field of electronics and energy storage. The continuous DIW process is among the most suitable AM candidates for the fabrication of electrical equipment such as integrated circuits, supercapacitors, electrodes, soft electronics, diodes, and even lithium-ion batteries at the micro-scale [51]. In large-scale, MEX has applications in additive construction, wherein a MEX head is equipped and mounted on a robotic solution [52]. To address the large scale of the prints, several mobile or stationary robotic solutions can be adopted, which are beneficial for additive construction in locations with limited accessibility or hazardous environments [49].

One of the current technological barriers of the MEX process, especially in FFF, is the limited availability of nozzle diameters on the market, with most diameters ranging between 0.15 and 0.5 mm [49]. Due to the diversity of applications presented by the technique and the aforementioned advantages, multifunctional structures, and specimens will be manufactured and studied in this work using FFF nozzles with a standard diameter of 0.4 mm.

2.1.2 Additive Manufacturing Design Aspects

In [43] the design aspects for AM can differ in geometric features and build parameters. In addition, the geometry of a part will be limited by the geometric continuity of its design, since parts are built layer by layer the material being deposited has the last layer built as support [43]. Therefore, if the material is deposited in mid-air, the resulting part may lose its integrity by presenting fabrication failures like deformation, porous mass, and reduced density [43]. Besides that, the build parameters are selected at the slicing phase and are also recognized as process parameters, so they affect the quality of the print and the time spent to finish a part.

The two design aspects mentioned have subcategories, however, only those referring to the build parameters will be addressed, which are those analyzed in this work in the study of mechanical properties of multifunctional structures produced by AM. Therefore, the covered build parameters are infill and wall thickness.

Infill is a parameter that plays a huge role in a part's strength, weight, and structure [49]. This parameter has two fundamental aspects: infill density and infill pattern. Infill density is the bulk of the inside of a part, in slicers this is usually defined as a percentage between 0 and 100, with 0% making a part hollow and 100%, completely solid [53]. Infill pattern is the structure and shape of the material inside of a part, it ranges from simple lines to more complex geometric shapes and can affect a part's strength, weight, print time, and flexibility [53]. In FFF, 14 common infill pattern options can be chosen in the slicing software, including grid, lines, triangles, tri-hexagon, cubic, cubic subdivision, octet, quarter cubic, concentric, zigzag, cross, 3D cross, gyroid, and lightning. Among these options, the triangle pattern contains lines in the XY-plane creating hexagonal patterns with triangles in between, which provides strength in these two directions and flexibility in the z-direction [53]. Figure 3 shows the infill difference in a sliced cube, wherein more triangles are printed with a higher infill density.

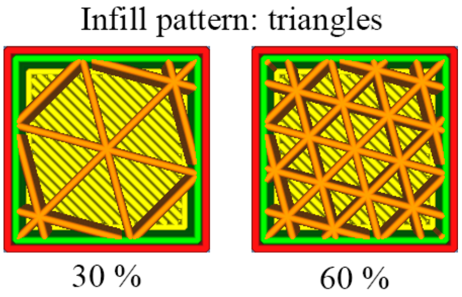

Figure 3 – Representation of different infill densities.

Wall thickness is a parameter that sets a minimum threshold on the thickness that is feasible to be manufactured [43]. This is due to the building threshold determined by the fundamental building unit used by every AM machine (in FFF is the extrusion nozzle) and the fact that the machine needs to make multiple passes to build a sufficient and solid feature [43]. As such, an integer multiple of the fundamental tool path width must be used for the design. When the geometry's width that must be manufactured is not an integer multiple of the fundamental tool path width, the slicer software will have to compensate for that issue [43]. Figure 4 shows the top view of a cube to exemplify how this parameter is controlled by the slicer. For a configuration in which the printing nozzle has a diameter of 0.4 mm and the wall thickness is 1.0 mm, the slicer calculates the same number of walls of a 0.8 mm thick print, so the third wall is only built when the thickness is set to 1.2 mm.

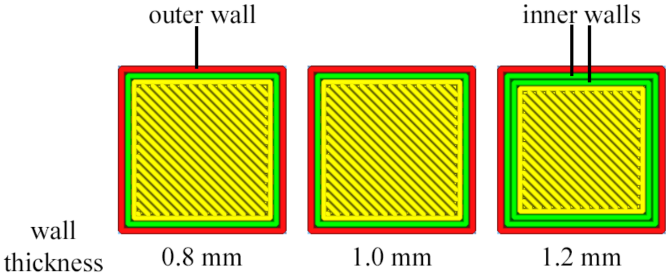

Figure 4 – Representation of different wall thicknesses in a sliced cube.

2.2 Optical fibers

Optical fibers have been used as electromagnetic waveguides, wherein they are making a significant impact in telecommunications that have spanned the earth and seas by kilometric extensions of cabling. The light-guiding characteristics of an optical fiber are mathematically described by Maxwell equations [54]. Using manipulations, considering a source-less medium, and assuming time-harmonic fields, the wave equation of an electric field propagating in z-direction is write

$$\mathrm{E} = \mathrm{E}_0 \exp\left[j(\omega t \pm \beta z + \phi)\right] \tag{2.1}$$

where $\beta = \omega/v = \omega n/c$ is the propagation constant of a sinusoidal wave measured along the z-axis, $v = 1/\sqrt{\mu\xi}$ is the wave velocity, μ and, ξ are the permittivity and permeability, respectively, of the medium [54].

The vector Helmholtz equations are the derived wave equation (simplified from the explicit form of time dependence Maxwell equations) in phasor form. In this approach, the wave vector K points in the direction of energy flow, and the propagation constant β is used to refer to the rate of accumulation of phase with distance for the electromagnetic wave [54]. Besides, this approach considers a plane electromagnetic wave in a uniform, linear, and isotropic medium of dielectric constant, where the propagation constant is β =k= $\omega n/c = n\mathrm{k}_0$ where $\mathrm{k}_0 = 2\pi/\lambda$, k= $\omega\sqrt{\mu\varepsilon}$, and λ is the light wavelength in vacuum [54]. Although, in a waveguide, each region i will be characterized by index n_i, so the magnitude of the wave vector in each region will be $\mid K_i \mid = n_i\mathrm{k}_0$, and the Helmholtz equations require a solution in each region with the matching boundary conditions at the interfaces [54].

An optical fiber needs at least two regions to guide an electromagnetic wave, which is known as core and cladding [55]. The simplest optical fiber to be manufactured is the step-index type, which has a single refractive index n_1 in the core, also to support a guide mode n_1 must be greater than n_2, the cladding refractive index [55]. In addition, β is constrained by the relation $n_2\mathrm{k}_0 < \beta < n_1\mathrm{k}_0$ since the mode propagates in both core and cladding.

The geometric approach uses Fresnel equations and Figure 5 exhibits how rays reflect and transmit at the interfaces, in this approach $\kappa_i = n_i\mathrm{k}_0 \cos\theta_i$ and $\beta = n_i\mathrm{k}_0 \sin\theta_i$ are referred as the transverse and forward propagation constants [54]. In this case, the electric field in each guiding region assumes the form $E_i \sim \exp(\mp j\kappa_i x)\exp(-j\beta z)$, but in the cladding region (2) κ_2 becomes imaginary, then it turns that the decay constant $\gamma_2 = j\kappa_2 = (\beta^2 - n_2^2 \mathrm{k}_0^2)^{1/2}$ is a real number [54].

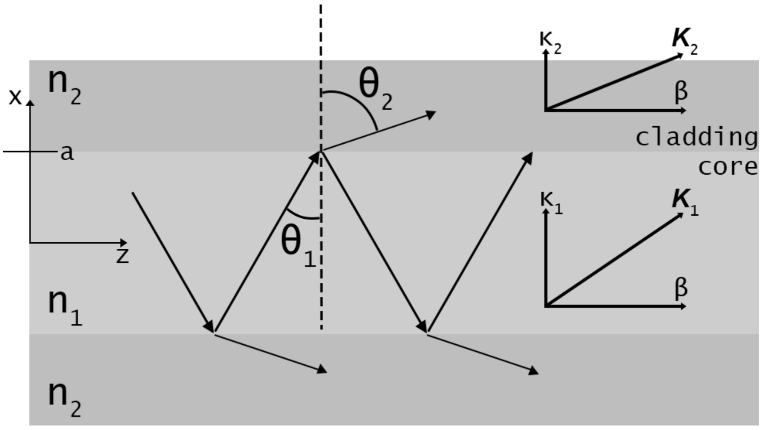

Figure 5 – Representation of the geometric approach of wave propagation along an optical fiber of core radius $r = a$. Reflections at the interfaces will follow Snell's law ($n_1 \sin\theta_1 = n_2 \sin\theta_2$) and total reflection occur when $\theta_1 > \theta_c = \sin^{-1}(n_2/n_1)$. Adapted from [54].

Therefore to form a propagating mode, the guided waves must be in phase after crossing the core. This includes the phase shifts caused by reflection on core and cladding interfaces, with a total shift being an integral multiple of 2π [54]. Besides, the phase shifts are determined from the Fresnel equations for the transverse electric (TE) and transverse magnetic (TM) cases, wherein these fields oscillate entirely in the transverse (xy) plane [54]. This generates a resonance condition that fixes the values of β and γ, leading to one or more guided modes that propagate along the z-axis, then it forms a standing wave along the x-axis in the core and decays exponentially in the cladding [54].

An outer layer is part of the composition of an optical fiber, the coating. It serves to preserve strength by protecting the glass surface from particles, providing some limited protection from environmental moisture, and mechanical protection from stresses that cause microbending losses [55].

An important feature presented in optical fibers is photosensitivity, which is defined as the capacity of a medium to have its refractive index permanently changed by a modification of its physical or chemical properties through light exposition [55]. In this context, the Ge-doped silica fiber core refractive index can be permanently modified by ultraviolet (UV) irradiation [55]. The first developed method is the holographic method, which consists of illuminating the core from the fiber's side with the interference pattern of two beams of coherent UV radiation imprinting FBGs [55]. However, the phase mask method simplified the fabrication of FBGs and permitted them to get longer gratings. In this method, a first static writing is made through the mask and the second with the translation of the UV beam through the mask into the fiber core [55].

The discovery of fiber photosensitivity led to the realization of optical components based on FBGs and encouraged new developments in both optical fiber communication and the optical fiber sensor field, the last is presented in Section 2.3. Besides, more details about FBGs and their formation mechanism are explained in Section 2.3.1.

2.3 Optical fibers sensors

As stated in Section 2.2, there are other fields besides communications where optical fibers are applied, such as optical fiber sensors (OFS) which is the application addressed in this work. The ability to manipulate characteristics of the electromagnetic wave, such as optical power and wavelength, inside the fibers makes it possible to apply OFS. In addition, the advantages of OFS over conventional electronic sensors include being intrinsically immune to electromagnetic interference (because fibers are made of dielectric materials), lightweight, compactness, multiplexing capability, and environmental ruggedness. Further, OFS is applied in structural health monitoring due to its multifunctional sensing capabilities [36]. That said, in [36] are presented different classifications for OFS, and they are based on

1. Working Principle - in this category the sensors are divided into intensity-modulated with detection through light power, phase-modulated with detection using the phase of the light beam, polarimetric detecting changes in the state of polarization of the light, and spectrometric with detection of changes in the wavelength shift;
2. Spatial Positioning - where sensors can be displayed in discrete points with a response for each sensor, distributed along a path (surface, or volume) providing spatial information or integrated along an optical link providing an average measurement of the perturbation over the sensing length of the fiber. Also, point and distributed sensors can be combined into quasi-distributed sensors, wherein the variable is measured at discrete points along an optical link;
3. Measurement Parameters - with OFS is possible to measure physical (temperature, strain, humidity, acceleration, pressure, acoustics, rotation), chemical, and biological parameters.

In addition, OFS can be divided into two basic classes referred to as extrinsic and intrinsic, and it depends on the transducer type. The extrinsic OFS consists of light in direct contact with the measurand so that the light leaves a fiber to come into contact with the measurand and is coupled into another fiber [35]. Intrinsic OFS rely on the light beam propagating through the optical fiber being modulated by the environmental effect either directly or through environmentally induced optical path length changes in the fiber itself [35]. A schematic of each class is shown in Figure 6.

The earliest type of OFS was the intensity-modulated sensors, and it is said that they are the simplest ones [36]. In these sensors, the transmitted optical signal has its intensity modulated

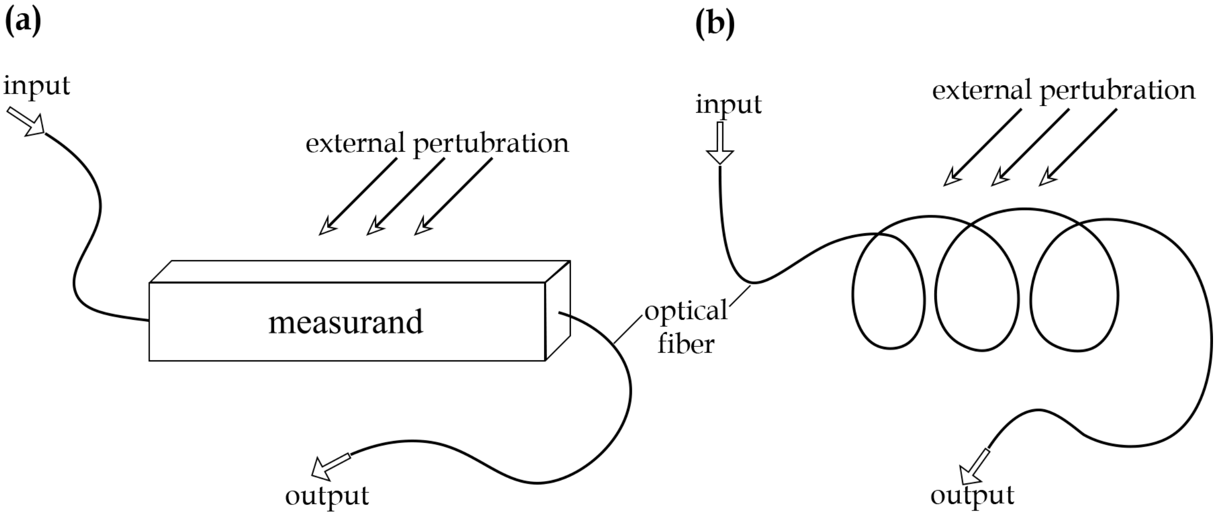

Figure 6 – OFS classes. (**a**) extrinsic and (**b**) intrinsic. Adapted from [36].

by various means such as fiber bending, reflectance, or changing the medium through which the light is transmitted [36]. Their advantages include ease of fabrication, simple detection system and signal processing requirements, and low-price performance [36]. However, their simplicity can cause optical fiber bending, coupling misalignments, and source power fluctuation, causing signal attenuation and signal intensity instability, which lead to a less reliable sensor system [36].

Phase-modulated sensors are also known as interferometric sensors [36]. Interference is a wave effect that can be observed in any type of wave whether it be electromagnetic, acoustic, elastic, or matter waves. In an optical fiber, the effect is based on a phase difference of coherent light traveling along two different paths, in the same fiber or different fibers [36]. These sensors are often considered high-sensitivity sensors due to their capability to respond to small changes in external measurement. The common interferometric sensors include fiber-optic Mach–Zehnder, Michelson, Fabry–Perot, and Sagnac interferometers [36].

Polarimetric sensors use the polarization properties of light propagating through an optical fiber, its state of polarization changes because of the difference in the phase velocity of the two polarization components in a birefringent fiber [56]. Birefringent optical fibers are fibers with anisotropic cross sections that have two distinct principle axes with different refractive indices, which are also called fast and slow axes [56]. Each axis has a different light velocity that depends on the polarization alignment of the incident light with one of the principle axes. Furthermore, in a polarimetric sensor, linearly polarized light is launched at 45° to both axes (such that both the polarization modes can be equally excited). The polarization state at the output is converted to intensity by using a polarizer–analyzer oriented at 90° to the input polarization state. Therefore, a change in polarization can be observed as a change in intensity, and by correlating the output change in intensity to the measurement [56]. Besides, the polarization properties of light propagating through an optical fiber can be affected by stress, strain, pressure, and temperature [56].

Spectrometric sensors are also called wavelength-modulated fiber sensors because they exhibit a change in the propagating optical wavelength when interacting with changes in the environment. One of the most widely used wavelength-based sensors is the Bragg grating sensor [36]. As explained in Section 2.2, FBGs are inscribed in an optical fiber by inducing periodic changes in the index of refraction in the core. There are other types of spectrometric sensors like fluorescence and blackbody sensors. Fluorescence sensors use a fluorescent material in the tip of the fiber, this material will emit more light and shift wavelengths when exposed to a radiation source [36]. In the blackbody sensor, a blackbody cavity is placed at the end of an optical fiber, and as the temperature of the cavity rises, it starts to glow and act as a light source [36]. Finally, since FBGs are the sensors employed in the produced multifunctional structures in this work, Section 2.3.1 is dedicated to explaining its theory and sensing principles.

2.3.1 Fiber Bragg grating sensors

Among the spectrally modulated fiber sensors, the most promising developments are those based on grating technology, the FBG. FBGs are mainly used in telecommunications as optical filters, dispersion-compensating components, and wavelength division multiplexing (WDM) systems. In addition, FBGs are sensitive to any perturbation of the fiber in the grating region and this led to extensive research to make use of it as a sensing element [57].

FBG is a periodic or quasiperiodic orthogonal perturbation of the refractive index along the longitudinal axis of the fiber core [57]. The grating structure acts like a selective mirror for the wavelength that satisfies the Bragg condition [57]. When an FBG is illuminated by a broadband optical source, a narrowband spectral component corresponding to the Bragg resonance wavelength of the grating, λ_B, is reflected, while all other wavelengths outside the narrow reflection band will be transmitted [57]. The Bragg wavelength, λ_B, is given by:

$$\lambda_B = 2n_{eff}\Lambda, \tag{2.2}$$

where Λ is the grating periodicity and n_{eff} is the effective refractive index of the waveguide mode [57]. The simplest form of an FBG is the uniform fiber gratings, as shown in Figure 7, where the phase fronts are perpendicular to the longitudinal axis of the fiber and the grating planes are of a constant period.

One method used in FBG fabrication is the phase mask. Phase masks are made up of period patterns usually etched onto fused silica [36]. That way, when the UV beam is incident on the mask, the zero-order diffracted beam is suppressed to less than a few percent of the transmitted power, and the diffracted ±1 orders are maximized, each typically carrying >33% of the transmitted power [36]. The rest of the power is divided into higher-order diffractions. For efficient diffraction into the first orders, a near-field fringe pattern with period $\Lambda = \Lambda_{pm}/2$ is produced by the interference of the beams [36]. The interference pattern photo imprints a refractive index modulation in the core of the photosensitive optical fiber placed close to the

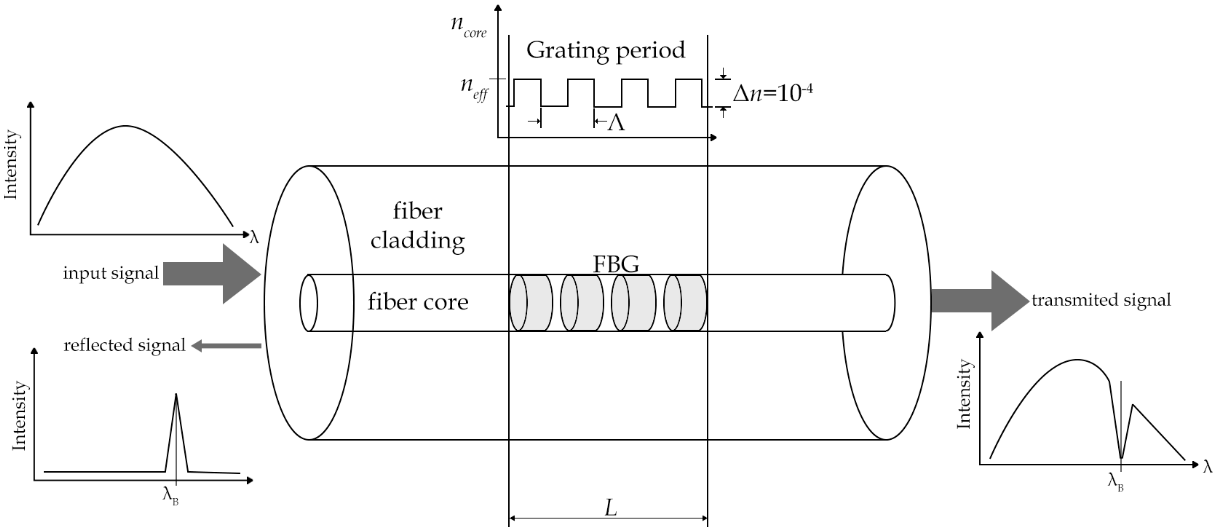

Figure 7 – Structure of a uniform FBG with constant index modulation amplitude and period. Adapted from [36].

phase mask. The period of the grating written in the core of the fiber is one-half of the phase mask period and does not depend on the wavelength of the writing beam or its incident angle on the phase mask, $\Lambda_{pm} = 2\lambda_B$ [36]. Therefore, to record a specific Bragg wavelength, a different phase mask can be used, and in the absence of this feature, a constant strain can be applied to the fiber to influence the recording periodicity of gratings. Figure 8 shows a schematic of the phase mask method to facilitate the visualization of this FBG fabrication method.

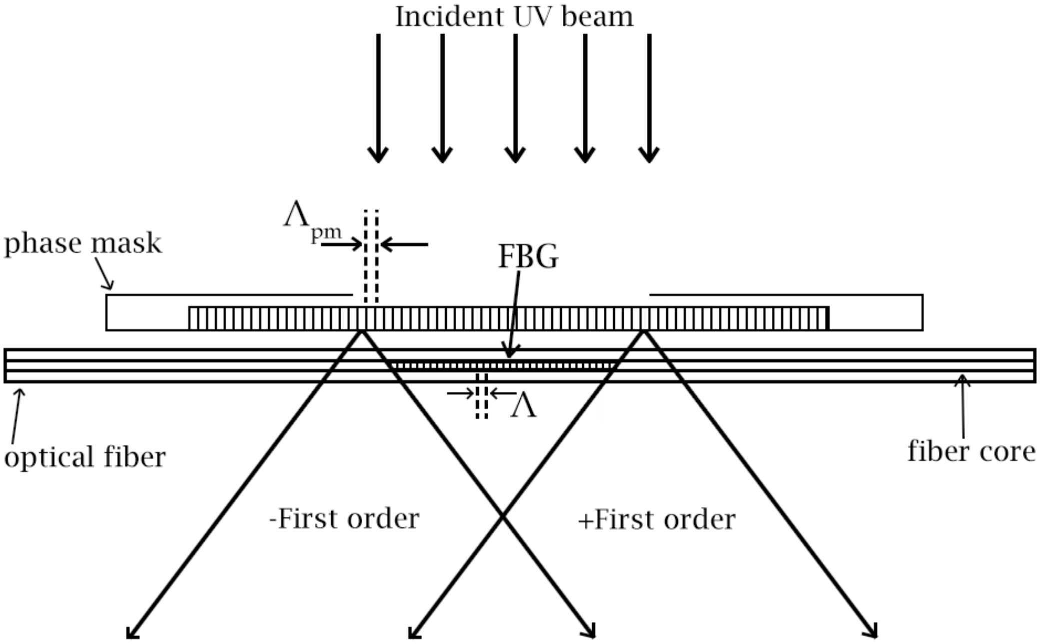

Figure 8 – Fabrication schematic of an FBG using a phase mask. Adapted from [36].

There are other manufacturing FBG methods. One of them is the transverse holographic technique, where 244 nm radiation is split into two and recombined to form an interference pattern in the fiber core, then this pattern induces a permanent localized index of refraction change [36]. The transverse holographic technique is one type of external inscription technique and other external fabrication methods were also developed, like amplitude splitting and the wavefront splitting interferometers [36]. The point-by-point method is said to be one of the more flexible methods in inscribing Bragg gratings, in this method, a UV source passes through a slit and then focused onto the fiber to produce an index change at one point, then the fiber is shifted a distance Λ which corresponds to the period of the Bragg condition [36]. Also, the writing of FBGs can be done using a femtosecond laser, such type of source is applied in the inscription methods by phase mask and the point-by-point [36]. Furthermore, the main advantage of high-energy pulses is their ability to inscription in any material type without preprocessing, such as hydrogenation or special core doping with photosensitive materials [36].

Just as there are different types of grating inscription, there are also different types of grating that specifically refer to the underlying photosensitivity mechanism by which grating fringes are produced in the fiber. Therefore, the fiber index change depends on UV intensity and UV irradiation dose. The physical attributes of gratings (sensitivity to high temperatures mainly) end up being affected by these different types of fringe creation as well. Among the types of FBG are Type I, Type IA, Type IIA, Type II, and regenerative grating [36]. A Type I FBGs are inscribed when the index modulation of the grating has a monotonic increase in refractive index, besides the index modulation n is between 10^{-4} to 10^{-3} [35]. Type IA FBGs use a similar inscription process to Type I, whose difference is a longer exposure time, and they have the same spectral characteristics as found in Type I gratings [36]. Type IIA grating has a blue shift in resonance wavelength during the formation, while Type IA presents a red shift in resonance wavelength [35]. When a UV pulse produces an index change near 10^{-2} the Type II grating is generated [35].

As explained previously, FBGs of different types can be manufactured by varying: the photosensitivity of the fiber, the type of radiation source used to inscribe the grating, and the time of exposure of the fiber to radiation during inscription. Furthermore, FBGs can present structures that vary with the periodicity of the gratings and the refractive index profile. Figure 9 shows some grating structures of single-mode silica fibers used mostly in optical fiber communications and fiber sensors. The uniform FBG is already shown in Figure 7, it has constants index modulation and period along the grating. It is also possible to inscribe two uniform FBGs in sequence, with the second having a phase difference from the first; this form of inscription produces the phase-shift FBG [35]. When the grating inscription produces a variable refractive index profile in a constant period, the structure is named apodized FBG [35]. However, if the variation is in the period of the inscription, the structure produced is the chirped FBG [35]. Finally, it is possible to inscribe the grating in a tilted direction from the fiber axis resulting in a tilted FBG [35].

What FBGs are and their different types were covered, it is now necessary to understand how they are applied in sensing, mainly addressing the sensing of physical parameters. By Equation 2.2, the Bragg wavelength variations are determined by both the sensitivities of the effective index and the grating period. Physical parameters like strain, temperature, surrounding

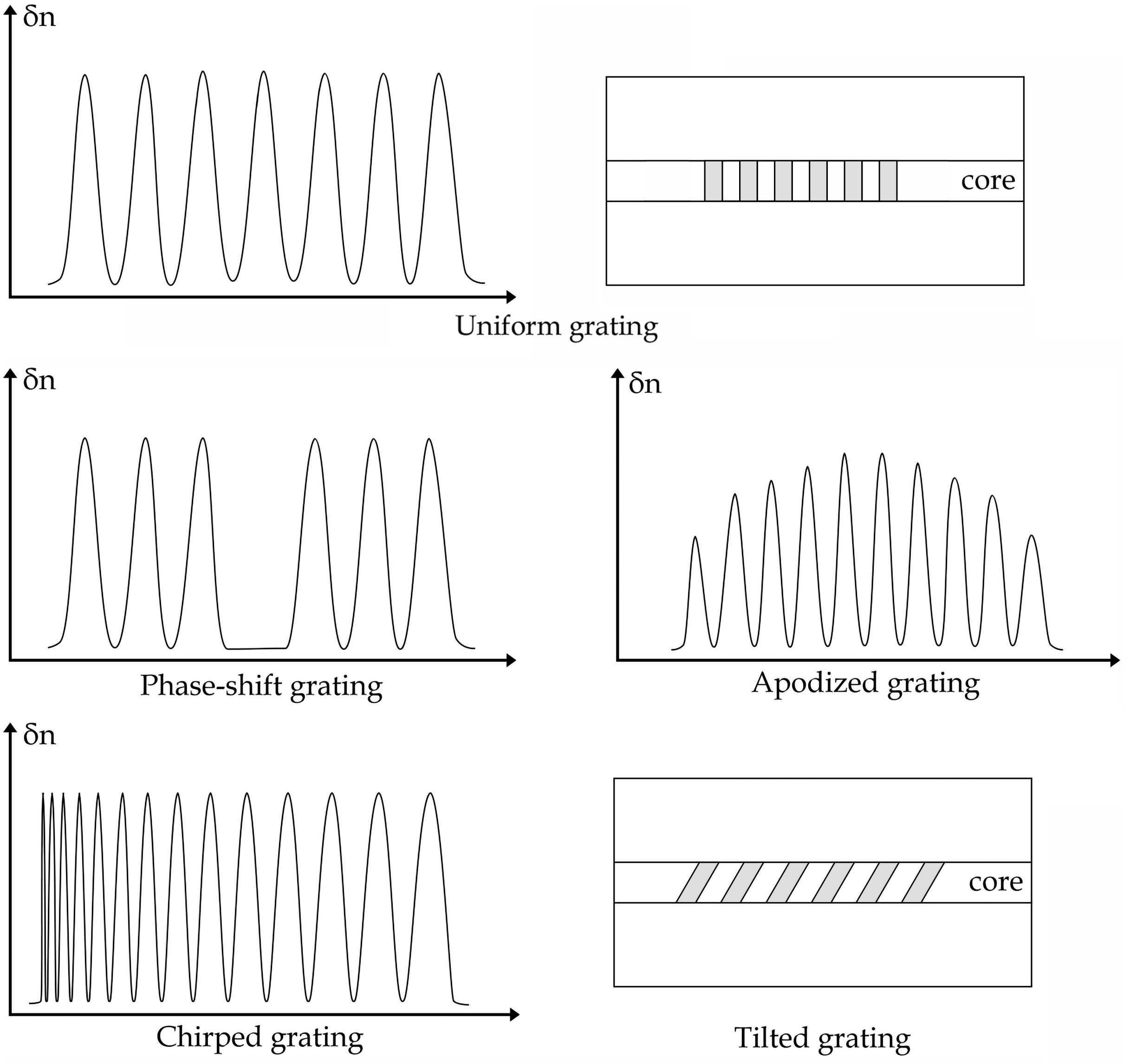

Uniform grating

Phase-shift grating

Apodized grating

Chirped grating

Tilted grating

Figure 9 – Distributions of refractive index and periodicity of the aforementioned FBG structures. Adapted from [35].

refractive index, displacement, and magnetic field are sensed by the FBGs due to their modulation of n_{eff} and/or Λ [36]. When an FBG is subjected to strain along its z-axis or thermally induced changes, the Bragg wavelength varies due to the change in Λ and the photoelastic-induced change in the n_{eff} [36]. The strain can be calculated separately when carried out at a constant temperature, thus the change in Bragg wavelength for a longitudinal strain is given by:

$$\frac{\Delta\lambda_B}{\lambda_B} = (1 - P_e)\Delta\varepsilon_z, \tag{2.3}$$

where P_e is the Pockel's coefficient of the strain-optical tensor and $\Delta\varepsilon_z$ is the applied strain [36]. It is important to note that the strain sensitivity of an FBG depends on the type of photosensitive fiber used to fabricate it as well as the diameter of the FBG containing fiber [58]. In addition, the wavelength shift for a temperature change can be written as:

$$\Delta\lambda_B = \lambda_B(\alpha + \psi)\Delta T, \tag{2.4}$$

where $\alpha = (1/\Lambda)(\partial\Lambda/\partial T)$ is the thermal expansion coefficient of the fiber and $\psi = (1/n_{eff})(\partial n_{eff}/\partial T)$ is the thermo-optic coefficient. Each FBG has a different thermal behavior. Some kinds of gratings can survive only at comparatively low temperatures of about 300°C and disappear after annealing for a few hours at temperatures over 350°C [59]. In addition, the thermal stability of the gratings is strongly dependent on the glass composition of the fiber into which the gratings are written. Moreover, special compositions of dopants incorporated into the fibers and the use of femtosecond infrared (fs-IR) lasers for writing the gratings have created FBGs capable of sustaining temperatures as high as 1000°C [60].

It is known that FBGs have direct sensitivity to strain and temperature, also, these parameters have an identical effect on the Bragg wavelength shift, so discrimination between the two variables is difficult. To overcome this, temperature compensation methods were developed, which are differentiated into intrinsic and extrinsic. In essence, FBGs themselves are used to discriminate the effects, the simplest form uses an FBG1 under the effect of the two parameters and an FBG2 (identical to FBG1) susceptible only to temperature variation, then with the wavelength shift of FBG2 it is possible to determine the deformation due to the temperature in FBG1 and, finally, calculate the strain due to the longitudinal load [36]. In extrinsic, the FBG is incorporated into a structure that has its material thermal expansion coefficient predetermined, so that the deformation of the FBG due to both parameters will be associated with the structure deformation [36].

FBG sensors are also used to measure the frequency of vibrations for structural health monitoring and damage detection applications. The basic working principle of an FBG vibration sensor is that vibrations induce high-speed dynamic strain variations in FBG, and consequently monitoring the shift in Bragg wavelength allows measuring those vibrations [36]. In addition, the FBG can be fixed onto a structure to tune the vibration effect, as Figure 10 shows a cantilever with one end clamped. The static deformation of a cantilever with transversely uniform sizes under a force F applied at its free end is described as:

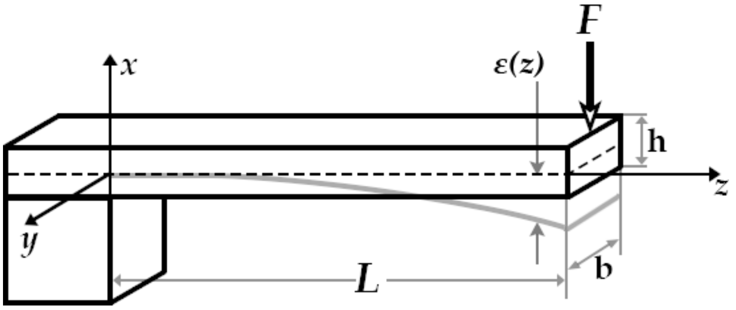

Figure 10 – Schematic of a cantilever. ε is the z-deformation of the structure when an x-direction force is applied on the free end. Therefore, an FBG fixed on the structure at $x = h/2$ will have a deformation represented by ε. Adapted from [35].

$$\varepsilon = \frac{F}{2EI}\left(L - \frac{z}{3}\right) z^2, \tag{2.5}$$

where Y is Young's Modulus and $I = bh^3/12$ is the moment of inertia about the y-axis [35]. Besides, the stiffness of the beam can be obtained using beam theory and is represented by $k = 3EI/L^3$ [61]. However, modeling the static deformation is insufficient to reproduce the vibration transmitted to the beam at the FBG. Vibration involves dynamics, so mechanical modeling based on harmonic motion is necessary to describe vibration in a cantilever. Then, by modeling the free-body diagram and considering the cantilever as a mass-spring system, the displacement of the cantilever free end is represented by $x = A\sin(\omega_n t + \phi)$, where A is the amplitude, is the system's first natural frequency, and ψ is the phase angle [61]. In addition, the natural frequency of the system is defined as:

$$\omega_n = \sqrt{\frac{k}{\frac{33}{140}m + M}}, \tag{2.6}$$

where M is a tip mass represented in Equation 2.5 by $F = Mg$, and m is the beam mass [61]. Therefore, the cantilever strain is transferred to the fiber, and the fiber strain results in a wavelength shift of the FBG, thereby it is possible to process the variation in the wavelength applying signal processing by using the the fast Fourier transform (FFT) [61]. The FFT is an algorithm used to convert a signal from the time domain to the frequency domain, allowing the analysis of its frequency components [61].

FBGs can be applied to measure various parameters; however, only those relevant to this work have been addressed. Leveraging the versatility and intrinsic characteristics of these sensors, the multifunctional structures manufactured will be embedded with FBGs to monitor parameters such as temperature, strain, angle, humidity, and vibration frequency.

2.4 Dynamic and static characterization of materials

In Section 2.4 the characterization techniques used to obtain mechanical properties of the materials used in the manufacture of multifunctional structures are discussed. The techniques presented are differentiated between static and dynamic, and the peculiarities of each are elaborated on in the following subsections.

2.4.1 Static characterization

Static characterization follows the ASTM D638 standard to obtain the tensile properties of materials through testing. These properties may vary with specimen preparation, as well as with testing speed and environmental conditions. This characterization involves different types of recommended test specimens, including sheets, plates, molded plastics, rigid tubes, and rigid rods [62]. The difference between them lies in the cross-section area. The type adopted in this work is shown in Figure 11, which falls under the category of sheets, plates, and molded plastics.

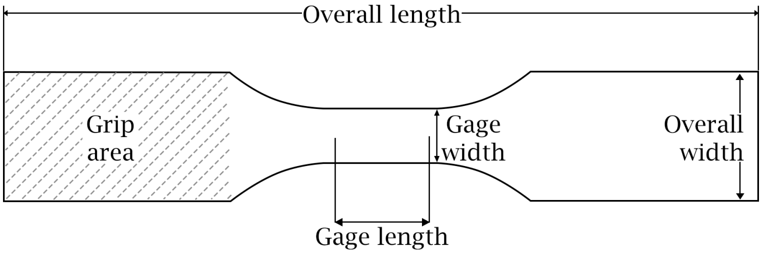

Figure 11 – Tensile test specimen model. Adapted from [62].

Another important parameter in the characterization is the test speed, which must be selected according to the table provided by the standard. This ensures that the specimen rupture occurs within a 0.5 to 5-minute range [62].

The basic operating principle of this technique involves applying stress (σ) to a specimen and analyzing its response. The response is measured in the form of strain (ε), enabling the estimation of a stress-strain curve for the tested material [62]. From this curve, it is possible to obtain other characteristics of the material studied, including the material's stiffness or Young's modulus (E). This can be calculated by dividing the difference in stress corresponding to a segment of the linear section on the curve by the difference in strain in the same section [62]. The value of E varies depending on temperature variation.

2.4.2 Dynamic characterization

Dynamic mechanical analysis (DMA) allows the characterization of bulk properties directly affecting material performance. Similarly to static characterization, it is possible to obtain E of dynamically tested materials. However, the calculation of E is only valid within a small range of strains on the stress-strain curves, specifically in the linear region of the curve. This behavior is easily observed in elastic materials such as ceramics, glass, or diamond [63]. Although, polymers are viscoelastic materials thus a stress-strain curve using the Hookean approach does not accurately represent these materials. With DMA, the complex (E *), elastic (E'), and imaginary (E") moduli obtained from the response of the material are measured [63]. Figure 12 illustrates the relationship between these moduli, where E' represents the material's ability to return energy, E"represents the ability to lose energy, and the ratio between these effects, tan delta (Tan δ), is referred to as damping [63].

In tests carried out to estimate the modulus of materials, shape factors must be considered, as small changes in geometry can result in a change in the calculated modulus value. This is because the force transferred from the machine over the cross-sectional area of the test specimen is calculated in the form of stress, $\sigma = F/A$. Due to this, the ASTM recommends the use of standard sample sizes for mechanical tests.

The temperature change in materials generates transitions in their moduli, which can be observed in the graphs generated. Figure 13 illustrates an ideal transition curve and the associated

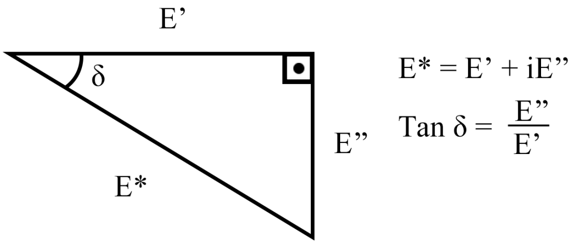

Figure 12 – Damping is calculated using the phase angle and amplitude of the signal. As the material becomes elastic, δ becomes smaller, and E* approaches E’. Adapted from [63].

molecular movements. The thermal transitions in polymers can be described in terms of free volume changes or relaxation times. The free volume of a polymer, denoted as v_f, is defined as the space a molecule has for internal movement. It is known to be related to viscoelasticity, aging, penetration by solvents, and impact properties. As the free volume of the chain segment increases, the atoms’ and molecules’ ability to move in various directions also increases, resulting in greater compliance (low modulus) of the molecule [63]. At very low temperatures, the molecules in a polymer are tightly compressed. As the material warms and expands, the free volume increases, allowing localized bond and side chain movements to occur. This transition is known as the gamma transition, denoted as T_γ. As the temperature continues to increase, the side chains and atoms gain enough space to move, resulting in some toughness. This transition is called the beta transition, and is denoted as T_β. As heating continues, the material reaches the glass transition temperature, indicated as T_g, where the chains in the amorphous regions begin to coordinate large-scale motions. It is important to note that T_g only occurs in amorphous materials. Finally, the melt transition temperature, denoted as T_m, is achieved, where large-scale chain slippage occurs, and the material flows [63]. Figure 13 shows an example scan of a polymer. The rubbery plateau is dependent on the molecular weight between entanglements (M_e) or crosslinks. The rubbery plateau is also related to the degree of crystallinity in a material [63]. This crystallization

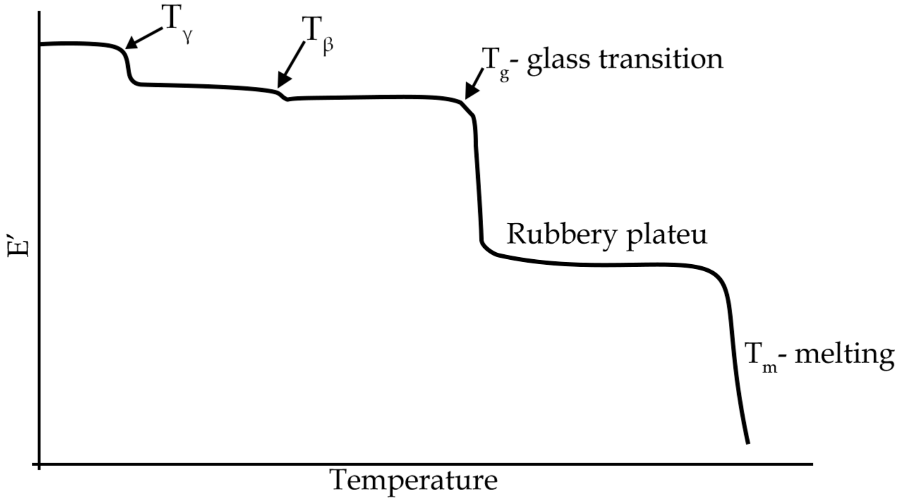

Figure 13 – Effect of temperature on the storage modulus in an example scan. Adapted from [63].

occurs when the polymer chains have been arranged into a highly disordered state, and then heat supplies energy to provide mobility to these chains [63].

Finally, the frequency at which materials are tested also has variable effects due to viscoelasticity. Depending on the frequency, these materials may exhibit flow or unrecoverable deformation. At low frequencies, a polymer can exhibit viscous or liquid-like behavior, while at higher frequencies, the material will behave elastically [63].

3 Methodology

Chapter 3 presents the methodologies applied to achieve the objectives of the work. It is divided into subsections, each dedicated to the characterization of materials and the different manufactured multifunctional structures. Within each subsection, the materials used, the tests performed on these materials, and the respective characterization will be presented.

3.1 Materials characterization

The characterization of materials is divided into static and dynamic characterization. The static mechanical characterization was carried out on the universal testing machine (MbioPDI, Brazil) following the recommendations of the ASTM D638 standard. In this procedure, five specimens are subjected to the stress-strain test to obtain their Young's modulus (E). The strain rate applied to the specimens during the test is 0.1 mm/min. The material subjected to the test is raw PLA filament, commonly used in additive manufacturing, and PLA embedded with an uncoated SMF-28 optical fiber (Corning, USA). The optical fiber embedding in the PLA specimens was carried out during their printing on the Ultimaker S5 3D printer (Ultimaker, Netherlands). For integration, the print was paused at half the height and the fiber was positioned in the body's center. So that it was well stretched when its ends were fixed with adhesive tapes on the printing table. Then, the printing of the bodies was continued until it was finished, observing the printer's extrusion nozzle, because if it collided with the fiber, another specimen would have to be printed. With printing coming to an end, the specimens proceed to characterization.

The main purpose of static mechanical characterizations is to assess the influence of filling and wall thickness variation on the modulus of elasticity of test specimens embedded with optical fiber. A layer height of 0.2 mm is adopted, and the same printing direction is maintained for all specimens. For the first tests, the wall thickness is fixed at 0.8 mm, while the infills are tested at 25%, 50%, 75%, and 100%. In addition, to assess the wall effect, the infill is kept constant at 50%, while the thickness varies between 0.4 mm, 0.8 mm, 1.2 mm, and 1.6 mm. Furthermore, the same tests are conducted on PLA specimens embedded with SMF-28 optical fibers to evaluate the change in their mechanical properties resulting from the embedding process.

The main purpose of dynamic mechanical characterization is to assess the modulus of elasticity at different vibration frequencies of the materials used in fiber-embedded cantilever accelerometers manufacture. With this module, it is possible to calculate the natural frequency of each system using Equation 2.6. The dynamic mechanical characterization was conducted with temperature variation using the Dynamic Mechanical Analysis (DMA) machine from Metravib (ACOEM, France). Dynamic tests were performed on nylon (Ultimaker, Netherlands) and Ultrafuse® 17-4 PH (BASF, Germany) specimens. As was done for the PLA specimens, the nylon and 17-4 PH specimens were manufactured on the Ultimaker S5 printer. The SMF-28 optical fiber was embedded without coating, and positioned in the center of the width and height. Tension clamps and a single cantilever were utilized in DMA. The mechanical load amplitude imposed during the tests was a displacement of 5 μm. Moreover, the specimens were excited at 1 Hz, 10 Hz, and 100 Hz. Considering the melting transition temperature of these materials, the temperature range for the tests varied accordingly. The initial temperature in the testing was set at 30 °C and was raised to 180 °C for nylon and 200 °C for Ultrafuse® 17-4 PH, respectively.

3.2 Artificial tendon embedded with FBGs

The material used to construct the artificial tendon is polyurethane (PU). PU is a thermosetting polymer formed by mixing polyols and polyisocyanate compounds, resulting in a flexible element. Before manufacturing the tendon, this polymer is subjected to static stress-strain testing to determine its modulus E before and after integration with the optical fiber. ASTM D638 recommendations are followed for this testing, which involves testing five specimens of each type: pure PU, PU with optical fiber, and PU with optical fiber and protection layer. The specimens are tested on a universal testing machine (MBioPDI, São Carlos, Brazil) under a deformation rate of 10 mm/min.

To manufacture the tendon, a mold with its shape was prepared to assist in positioning the FBGs, and then the viscous PU was poured to fill it. This positioning of the FBGs was chosen to verify whether the strain sensitivity is affected by the eccentricity of the fiber. Therefore, the mold prepared and manufactured with FFF has an internal diameter of 4.5 mm (the final diameter of the tendon), and the eccentric fibers are positioned on opposite sides at a distance of 1.25 mm from the center. Figure 14 shows the setup used to manufacture the tendon and position the FBGs. Manufacturing is completed with the resin completely cured after 24 hours of mixing the PU compounds.

The tendon undergoes temperature, longitudinal strain, and curvature characterizations. For temperature characterization, the tendon is placed inside an oven (Ethik Technology, Vargem Grande Paulista, Brazil) and subjected to a temperature range of 30 °C to 60 °C in 5 °C increments. In this tested temperature range, the PU is on the rubbery plateau (as shown in Figure 13) and it is expected that in this range there will be no magnitude variations in the mechanical resistance of the PU. The wavelength of the FBGs is acquired using a si155 optical interrogator (Luna Innovations, Roanoke, VA, USA) at a rate of 10 Hz for 1 minute, after 30 seconds of the oven temperature stabilization.

Longitudinal strain characterization is performed on the FBGs before integration, and the same procedure is repeated on the tendon after integration. For this characterization, the fibers with FBGs and the tendon are fixed at both ends, with one end secured in a linear stage with an accuracy of 10 μm. The initial length of the fibers and tendon is measured to calculate the

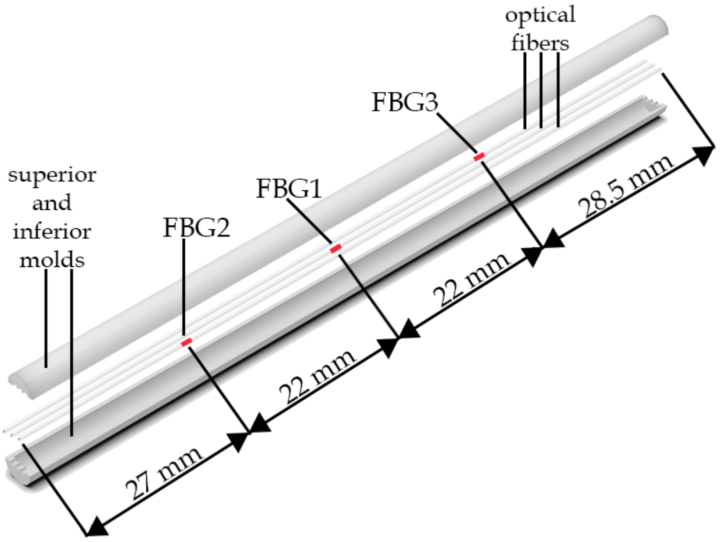

Figure 14 – Setup used in the manufacture of the artificial tendon.

engineering strain (ε). Signal acquisition in these strain characterizations is performed by the optical interrogator at an acquisition rate of 500 Hz for 30 seconds. The applied strain range varies from 0 μm to 100 μm in increments of 10 μm.

The final characterization performed on the tendon was the curvature, with the tendon subjected to an angular range from 0° to 90° in 15° increments. Figure 15 shows the setup used in the experiment. This characterization takes into account the variation in the power of the optical signal, as well as the Bragg wavelength shift.

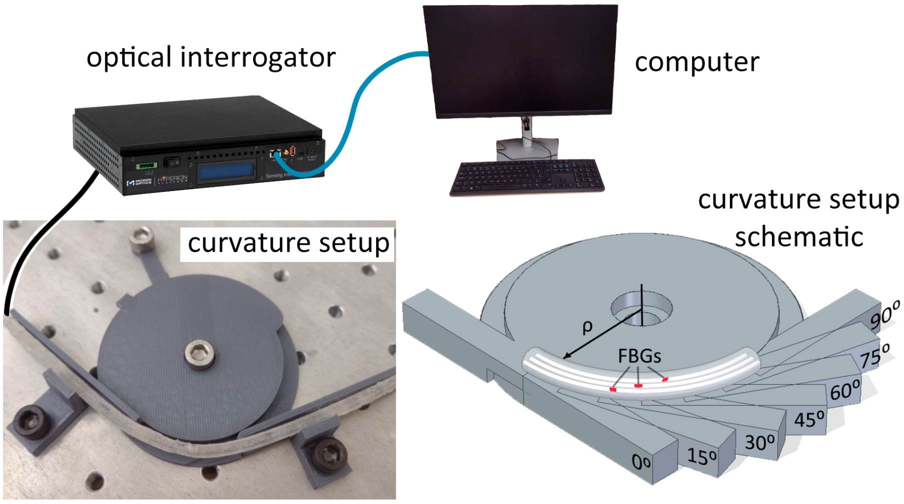

Figure 15 – Experimental setup used in the curvature characterization of the artificial tendon.

3.3 Temperature sensor

Sensing applications aimed at industry can be included within the Industry 4.0 concept, in which equipment is automated and connected to a network providing data during control operation. This information is also useful for structural monitoring of equipment. It can include sensors for measuring deformation, temperature, and vibration frequency, which signal the equipment's operating state and useful life. In this context, equipment can be incorporated with sensors to provide data of interest for automating processes, as well as for monitoring useful life. This incorporation of sensors can be facilitated by 3D printing through the manufacture of parts adapted for each piece of equipment. Then, optical fiber sensors, which are light and compact, can be embedded in these parts manufactured by printing.

In the specific case of temperature measurement, the direct sensitivity of the Bragg wavelength to temperature variation has already been well-defined in several studies. However, FBG is also sensitive to deformation, and considering an industrial environment, where deposited solid particles or gases capable of chemically interacting with the optical fiber may cause deformation at the FBG location, resulting in a temperature measuring error. Therefore, the aim is to embed the FBG sensor within a chemically stable resin structure to isolate the temperature parameter and enable temperature measurement in any type of environment.

The temperature sensor is manufactured using the photo-cure resin Basic Clear (Anycubic, Shenzhen, China), and the structure is printed on the 3D printer Photon Mono X 6K (Anycubic, Shenzhen, China). After printing, the optical fiber with FBG sensor is positioned inside a hole in the structure, which is then filled with resin and cured to fix the fiber in place.

The first test was conducted to verify the variation in Bragg wavelength (λ_B) when the structure is exposed to humidity. In this test, the structure is immersed in a container filled with water at a constant temperature, and the optical signal of the λ_B peak is acquired by an optical interrogator si155 (Luna Innovations, Roanoke, VA, USA) at a rate of 1 kHz for 3 minutes. Finally, a test is conducted to verify the relationship between the variation in λ_B and temperature. The structure is exposed to temperature variations between 25 °C and 40 °C in increments of 5 °C, with different relative humidity levels (50%RH, 60%RH, 70%RH, 80%RH, 90%RH). This test is carried out inside a climatic chamber Q315C21 (Quimis, São Paulo, Brazil), and the optical signal is acquired using the same interrogator mentioned above at a rate of 500 Hz for 1 minute each temperature. The setups and materials used in both tests are shown in Figure 16.

3.4 Accelerometer cantilever

The accelerometer cantilevers were produced using the Ultimaker S5 3D printer employing two distinct filaments, nylon (Ultimaker, Netherlands) and Ultrafuse® 17-4 PH (BASF, Germany). Optical fibers inscribed with FBGs were embedded during the printing process. Then, the structures were characterized using a vibration generator (TIRA, Schalkau, Germany), which applied a displacement to the structures in a sine waveform through the arbitrary function generator AFG3021C (Tektronix, Beaverton, USA). The generated signal was amplified by the BAA 120 signal amplifier (TIRA, Schalkau, Germany).

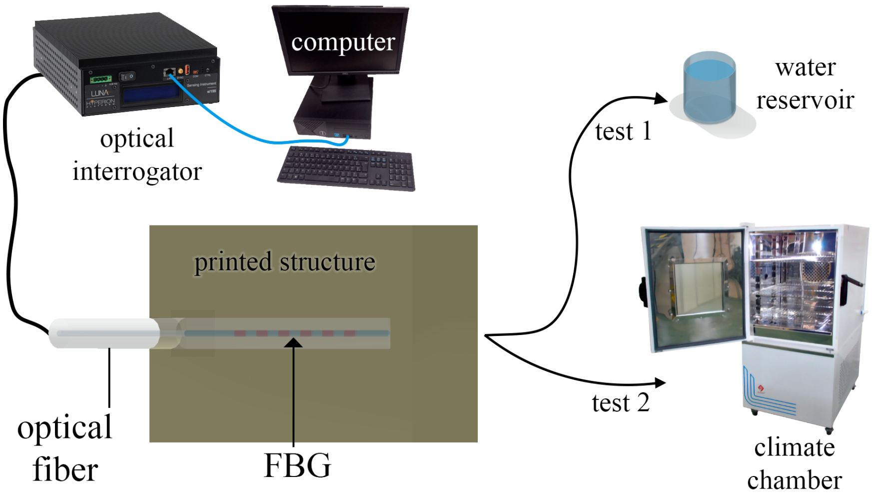

Figure 16 – Experimental setups used in temperature sensing structure.

The cantilevers were characterized at frequencies of 10 Hz and 100 Hz. For characterization, the amplitude of the amplified signal varied from 0.5 V to 2.0 V in intervals of 0.3 V, while the current was fixed at 0.1 A. The vibration response of the cantilevers (i.e., the FBG signal) was captured for 5 minutes using the si255 optical interrogator (Luna Innovations, Roanoke, VA, USA). This interrogator has an acquisition rate of 5 kHz. The setup used to characterize the cantilevers is shown in Figure 17.

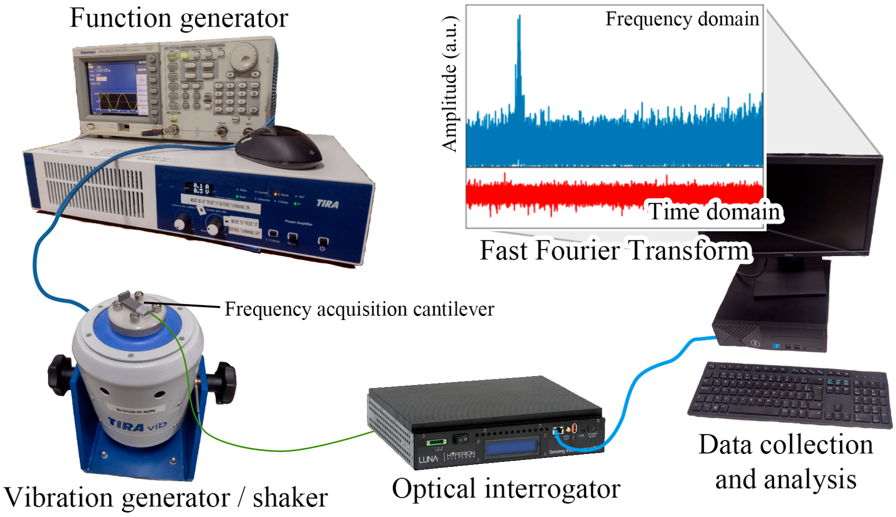

Figure 17 – Experimental setups used for frequency acquisition cantilever structure.

4 Results and Discussion

Chapter 4 presents the results obtained from the tests and characterizations, along with a discussion of these results. The chapter is structured similarly to Chapter 3 to organize the presentation of the results.

4.1 Materials characterization

The results of the static mechanical characterization are presented in Table 1. Since five specimens were tested, the E values displayed in the tables represent the average of these tests for each specimen configuration.

In Table 1 (a), an increasing trend is observed in E as the filling and wall thickness increase. This trend occurs as the filling and/or wall thickness increase because of the greater amount of material in the cross-section along the body. Consequently, the density of material in the cross-sectional area of the body increases. As a result, more mechanical effort is required to cause deformation in the material due to this increase.

Infill (%)	**E (MPa)**	**Wall (mm)**	**E (MPa)**
25	1140.97	0.4	1174.99
50	1118.42	0.8	1118.42
75	1263.07	1.2	1289.36
100	1332.84	1.6	1403.93

(a)

Infill (%)	**E (MPa)**	**Wall (mm)**	**E (MPa)**
25	1416.92	0.4	1333.88
50	1288.31	0.8	1288.31
75	1402.42	1.2	1441.48
100	1368.10	1.6	1423.48

(b)

Table 1 – Test results of the PLA specimen. **(a)** exhibit test results of raw PLA specimens, and **(b)** shows the PLA embedded with an optical fiber.

Table 1(b) displays the results of the tests carried out with PLA embedded with optical fibers. In contrast to the previous results, there is no variation in the E value between different configurations. This lack of variation is attributed to the optical fiber module, which exceeds that of PLA and polymers in general. As a result, the mechanical resistance of the test piece is primarily influenced by the resistance of the fiber. Consequently, embedding optical fibers can enhance the mechanical resistance of polymeric materials used in additive manufacturing. In essence, a greater predominance of fibers in the cross-sectional area leads to the specimen modulus approaching that of the fiber modulus.

The dynamic mechanical characterization results are illustrated in the following figures. Figure 18 presents the results obtained from tests performed on nylon using tension clamps. Initially, at lower temperatures, nylon undergoes a glass transition until it reaches approximately

60 °C. During this phase, typical of amorphous polymers, the nylon polymer chains possess free spaces to move until their structure becomes more ordered. This transition is marked by the flatter region of the modulus curve in Figure 19, occurring between 75 °C and 160 °C. Beyond 160 °C, nylon begins to flow viscously, resulting in a continuous decrease in mechanical strength.

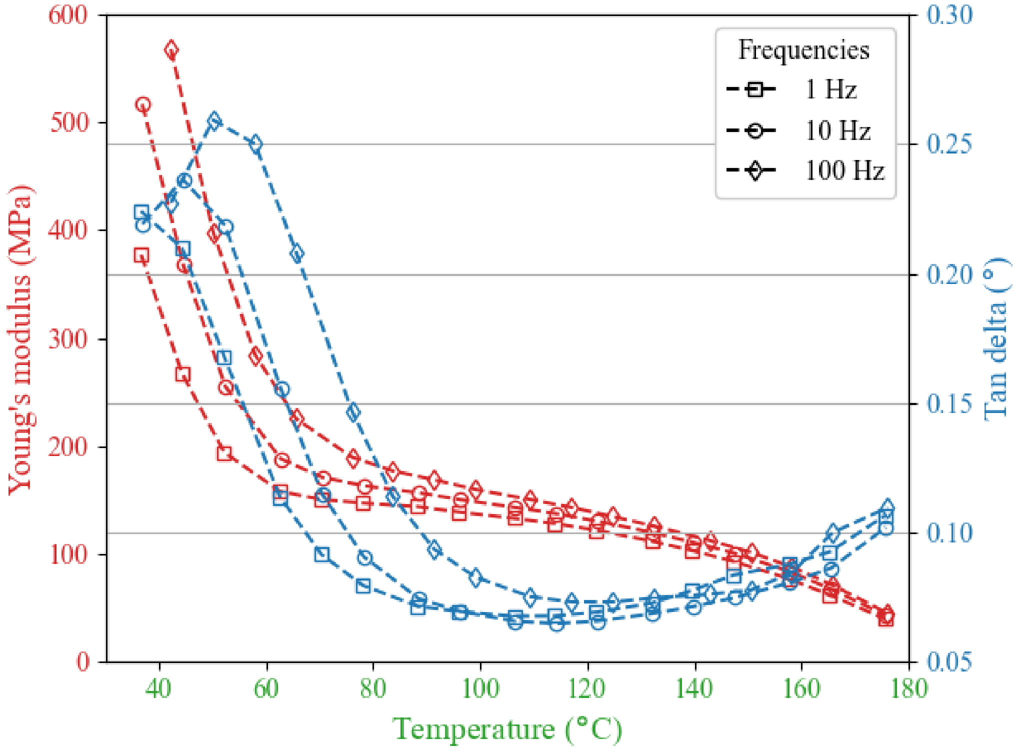

Figure 18 – Results of nylon test piece with an internal filling of 25% and a layer height of 0.2 mm.

Another notable characteristic of this material is the increase in mechanical resistance as the frequency of displacement applied to the specimens rises, during the glass transition. This phenomenon may be attributed to the random molecular structure of nylon, which randomly occupies free spaces, making it challenging for the material's polymer chains to move. Consequently, more energy is required to facilitate movement. In Figure 18, the Tan delta (°) value tending to zero in the flat region indicates that the body exhibited almost purely elastic behavior during this phase. This result may be influenced not only by the ordered structure of the polymer but also by the presence of the embedded optical fiber in the test piece. Optical fibers are considered fragile materials that primarily exhibit elastic behavior.

Figure 19 displays the results of the single-cantilever test conducted on the Ultrafuse® 17-4 PH metallic filament in the temperature range of 120 °C to 200 °C. In contrast to previous findings, the resistance of this filament decreases throughout almost the entire temperature range used in the test, with a brief plateau observed in the temperature range between 180 °C and 200 °C. Additionally, it is noted that Young's modulus is greatly affected by temperature variation, presenting values above 600 MPa when the material is at 120 ℃, and decreasing to values close to 2 MPa at the plateau.

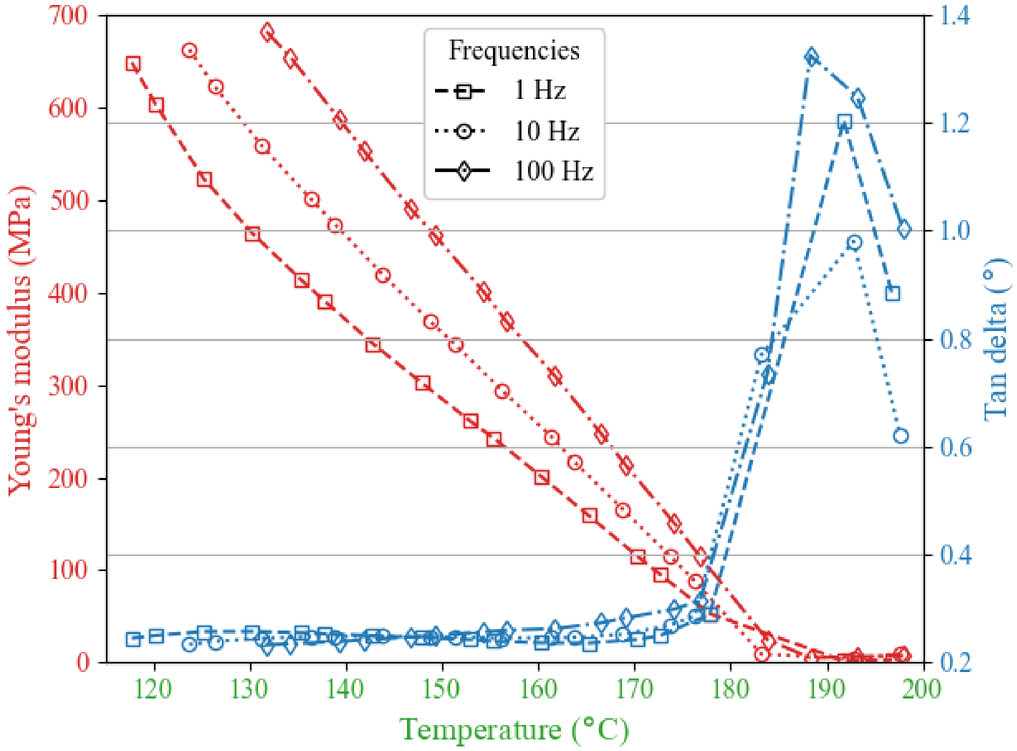

Figure 19 – Results of the single-cantilever dynamic test with Ultrafuse® 17-4 PH specimens with a layer height of 0.1 mm and 100% filling.

Moreover, the values of the Tan delta (°) in Figure 19 are closer to 0 ° during the transition, a different behavior from what was observed in Figure 18. This phenomenon suggests that the body exhibits almost purely elastic behavior during this transition. Furthermore, Ultrafuse® 17-4 PH, being an agglomerate composed of polymer and metal, possesses weaker bonds between its molecules for temperatures greater than 180 ℃. Consequently, parts made with this material may be fragile if the post-processing recommended by the manufacturer is not carried out.

4.2 Artificial tendon embedded with FBGs

Before characterizing the multifunctional structure of the artificial tendon, the PU (tendon material) underwent stress-strain testing in various configurations, as shown in Figure 20. The characterization results are presented in Table 2, where a difference in the mechanical resistance of the material is evident when integrated with the SMF-28 optical fiber. The elastic modulus for the PU material alone is measured to be 4.01×10^{-2} GPa. When the PU is integrated with an SMF-28 optical fiber, the modulus of elasticity slightly increases to 3.13×10^{-1} GPa. Furthermore, when considering the additional coating layer on the fiber, the modulus of elasticity further increases to 3.93×10^{-1} GPa. These values demonstrate the effect of optical fiber integration on

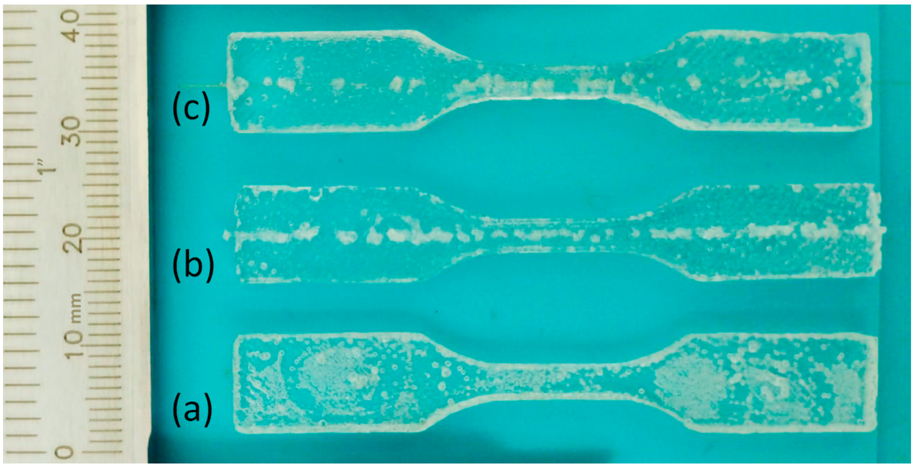

Figure 20 – PU test specimens. (a) PU, (b) with optical fiber, and (c) with optical fiber and coating.

Material	**E (GPa)**
PU	4.01×10^{-2}
PU and optical fiber	3.13×10^{-1}
PU, optical fiber, and coating	3.93×10^{-1}

Table 2 – Stress-strain test results of PU specimens.

the mechanical characteristics of the PU material, since the fiber E is around 70 GPa, leading to an increase in the artificial tendon E. It is also important to mention that the optical fiber also affects the strain limits on the artificial tendon, where there is a reduction in the strain limit when the optical fiber is integrated into the PU matrix. To that extent, Figure 21 shows the stress-strain curve of each configuration of the PU test specimens of Figure 20, in which it is possible to observe the region where there is a breakage of the optical fiber without coating, leading to a sharp decrease in the stress response. For this reason, considering that the artificial tendon will be embedded with fibers recorded with FBG and that recoating will not be done in the FBG region, it is possible to infer the influence of the optical fiber on the PU mechanical properties since there is a 37.45% reduction in the stress when there is optical fiber breakage in the stress-strain test. Furthermore, in specimens with coated fiber tested, the universal testing machine tension claws lost their grip on the bodies and started slipping. In Figure 21, the result of one of these specimens is seen, in which a line indicating the slipping was drawn, which after the continuation of the test becomes unfeasible because the grippers will not be able to continue pulling the specimens. The slipping occurs due to high stress in PU material during the test, as seen in the raw PU result it has low stiffness, which means that a higher stress applied in the material will present a higher deformation, leading to the grip loss.

Figure 22 presents the results of the strain characterization for three different FBGs. The x-axis represents the strain variation, calculated as the ratio between strain and initial length ($\Delta\varepsilon/L_0$). Each measurement has a step $\Delta\varepsilon$ of 10 μ m, and the measured L_0 values are 214.4 mm, 210.0 mm, and 195.0 mm for FBG1, FBG2, and FBG3, respectively. The y-axis represents

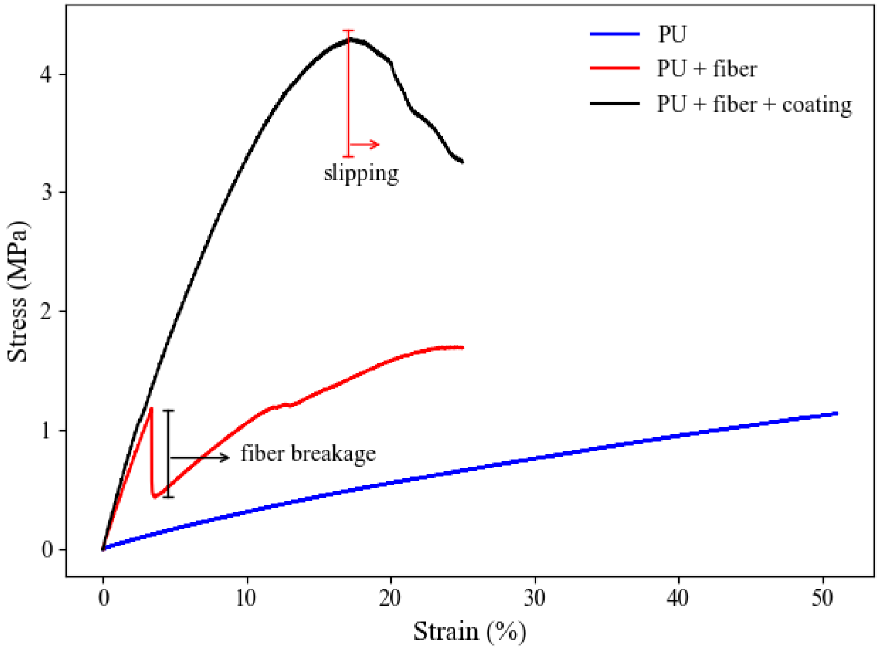

Figure 21 – Stress-strain curves of PU specimens.

the difference between the average wavelength value obtained in each measurement and the average value obtained in the first measurement. In each measurement, the total data collected for each FBG reached approximately 15000 values of wavelength. From Equation 2.3, the estimated relationship between the variables is linear, and then linear regressions were performed and shown by the straight lines in Figure 22. Therefore, the determination coefficient (R^2) that the FBGs presented was above 0.99, calculated for the advance and return results. Furthermore, the sensitivity (S) of the FBG directly depends on how much the gratings move when the optical fiber is deformed. In this way, as the same fiber material was used for recording the FBGs, the value of S differs only in the order of 10^{-2} pm between the tested ones.

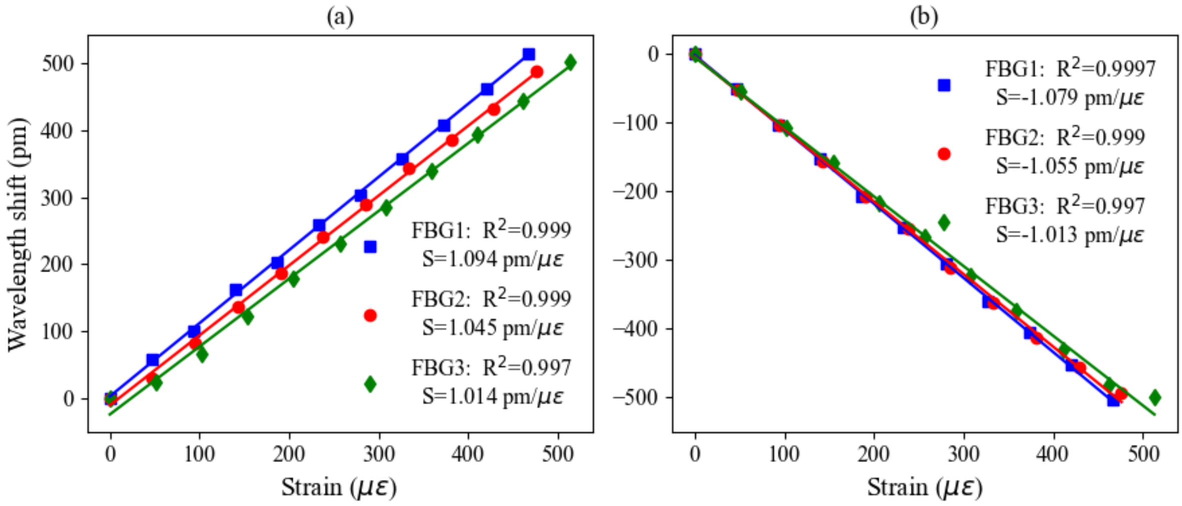

Figure 22 – Bare FBGs strain results: (a) increasing strain, (b) decreasing strain.

Figure 23 presents the results referring to the strain characterization in the FBG-embedded artificial tendon. The same variables represented in Figure 22 are on both axes but with the difference that the L_0 value was measured at 99.5 mm for the tendon. It can be seen in Figure 23 that FBG1 has an S value of 0.647 pm/$\mu\varepsilon$, while FBG2 and FBG3 exhibit an S value closer to 0.24 pm/$\mu\varepsilon$. This difference in sensor response is due to the positioning of the FBGs within the tendon, while FBG1 is positioned in the center of the cross section, the other two FBGs are displaced with the same eccentricity. When strain is applied in the longitudinal direction, the material is compressed in the transverse direction. Therefore, sensors closer to the end of the tendon (FBG2 and FBG3) are subjected to a stress field different from the sensor located in the center. The tests were sequentially performed with three cycles for each component and resulted in standard deviations of 36.02 pm, 13.19 pm, and 14.91 pm for FBGs 1, 2, and 3, respectively. Such results indicate a high repeatability of the proposed multifunctional structure.

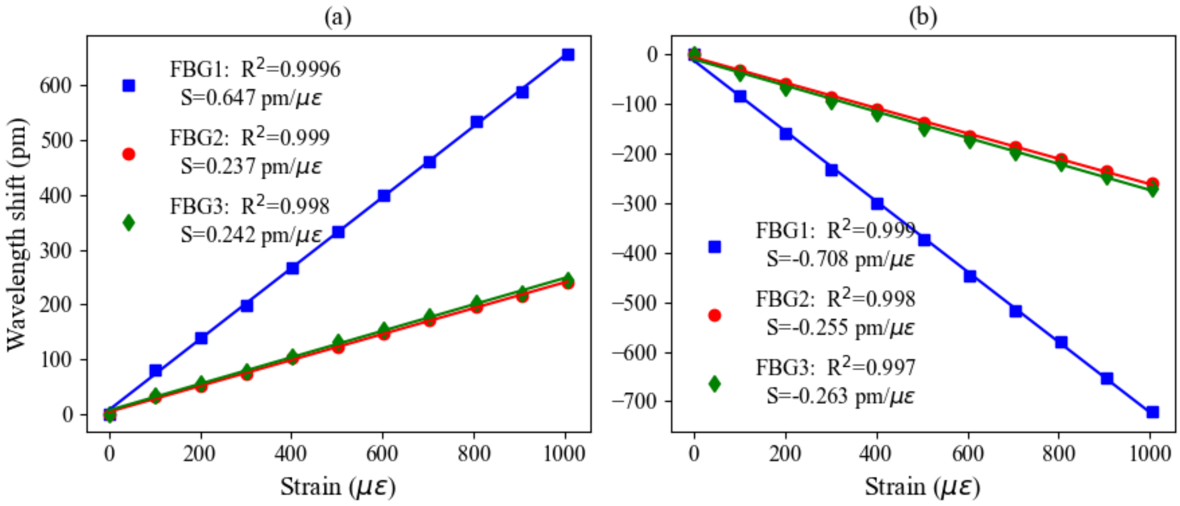

Figure 23 – FBG-integrated artificial tendon strain results: (a) increasing strain, (b) decreasing strain.

Figure 24 presents the results of the temperature characterization performed on the tendon. As seen in Equation 2.4, the relationship between temperature and wavelength shift in FBGs has a linear behavior. It can be observed with the determination coefficients that this relation does not change with the embedding of the sensors in the tendon. It is noteworthy that the sensitivity of FBG sensors to temperature variation depends on the heat conduction of the PU. Therefore, the presence of heterogeneity resulting from the fabrication of the tendon is a factor that influences the temperature profile within the material. For this reason, the position of the sensors within the tendon results in differences between their responses.

The last characterization test on the artificial tendon embedded with FBG is presented in Figure 25(a), where it is possible to observe the FBGs' reflected spectra at different angle conditions. To that extent, it is possible to observe the variations in the spectral features as a function of the applied angle on the tendon. In this case, there is a higher variation in the reflected

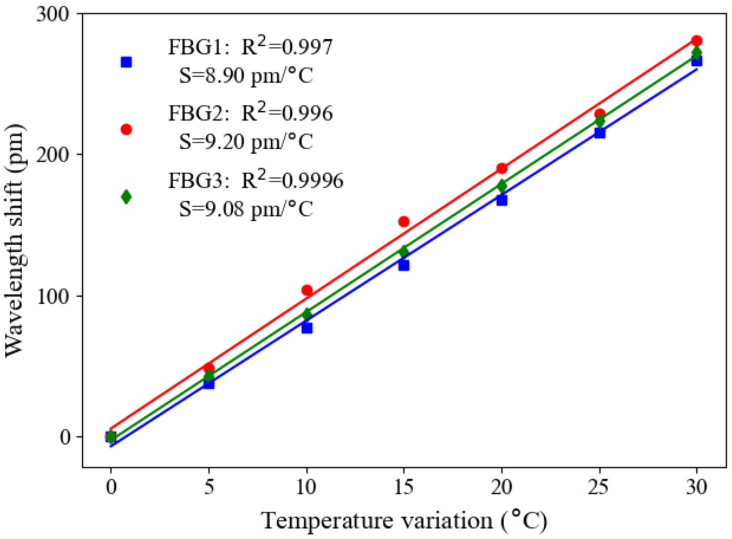

Figure 24 – FBG-integrated artificial tendon temperature results.

optical power related to the macrocurvatures applied to the optical fibers. It is important to mention that the bending in the fiber (especially in the FBG region) leads to different spectral variations in the sensor response, which is related to the specificity of such mechanical loading. In this case, there is a distributed quadratic strain along the tendon (and the embedded optical fiber) as demonstrated in [37]. Moreover, the optical attenuation induced by the bending of the optical fiber leads to a variation in the reflected optical fiber. For this reason, the wavelength shift and the optical attenuation of all three FBGs are used on a multi-feature regression model for the curvature angle estimation.

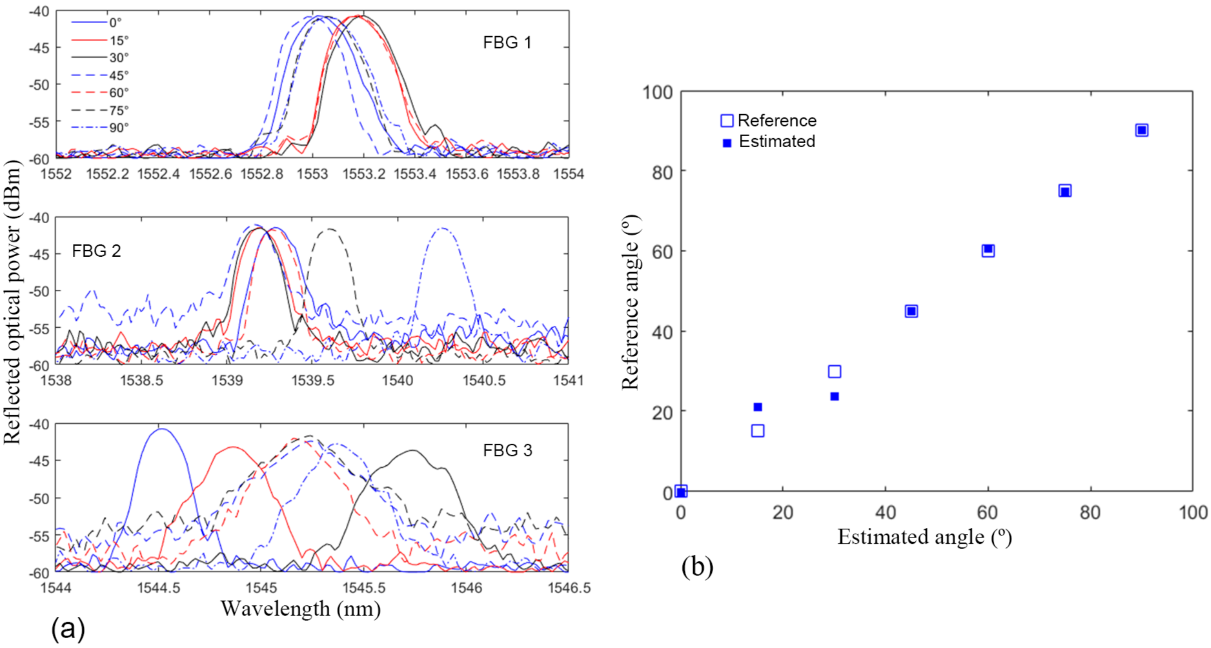

Figure 25 – FBG-integrated artificial tendon curvature results: (a) wavelength shift, (b) estimated angle.

$$\alpha_{1-3} = a_{1-3} \times \Delta\lambda_{B_{1-3}} + b_{1-3} \times \Delta P_{1-3} + c_{1-3} \times \Delta\lambda^2_{B_{1-3}} + d_{1-3} \tag{4.1}$$

$$\alpha_{est} = x_1 \times \alpha_1 + x_2 \times \alpha_2 + x_3 \times \alpha_3 + x_4 \tag{4.2}$$

In this case, the curvature angle is estimated from the reflected optical power and the wavelength shift as a function of the angle, where its variations for each FBG can be observed in Figure 25(a) in one of the three tests. Thus, the wavelength shift and the optical power variation are used in a polynomial relation to obtain the curvature angle, where such a relation can be used for each FBG. Then, all three estimated angles are combined into a single angle estimate using a linear relation as shown in Equations 4.1 and 4.2 for the angle estimation of each FBG and angle estimation combination, respectively. In addition, Figure 25(b) shows the estimated and reference angles considering all three FBGs of the proposed artificial tendon embedded with FBGs, where both optical power variation and wavelength shift are used in a polynomial regression. From the data of reflected optical power and wavelength shift of the embedded FBGs, it is possible to infer the bending angle and its direction from the spectral feature variations with a root mean squared error of around 3.25 °. In addition, the strain distribution along the tendon can be estimated from the strain results of each FBG embedded in the proposed artificial tendon.

4.3 Temperature sensor

Figure 26 (a) shows the variation of FBG λ_B when the structure is submerged in water. During the test, the water temperature is measured using a thermocouple to ensure that the variation in wavelength did not occur due to the variation of this parameter. It is noticeable that the resin material can absorb moisture, as indicated by the variation in λ_B when the structure is submerged. The wavelength varies until the material becomes saturated, indicated by the asymptotic behavior of the optical signal over time. Since the test temperature is constant, it is assumed that the variation in λ_B is due to the deformation caused in the fiber when the structure absorbs water.

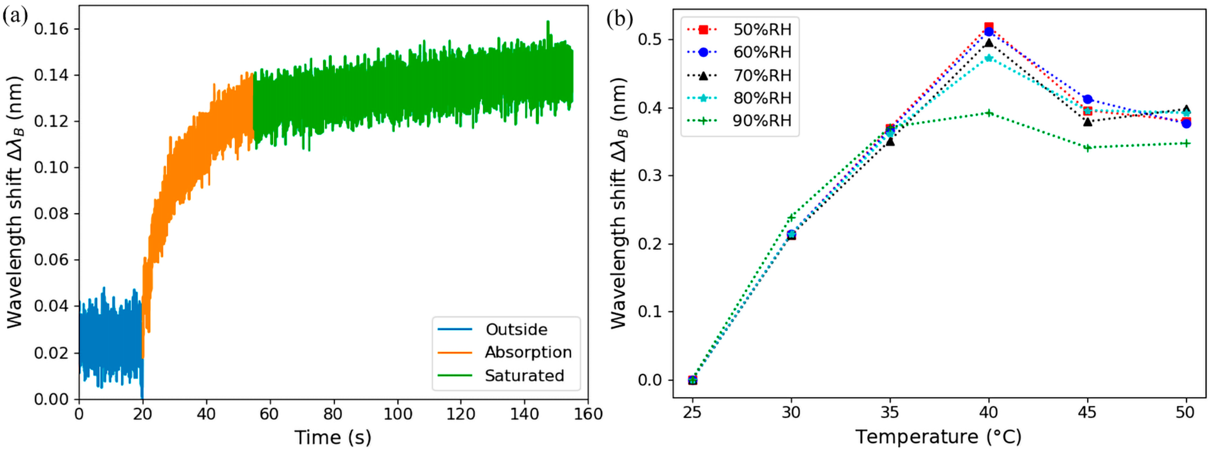

Figure 26 – FBG response in the tests. (a) Response of the structure submerged in water and (b) inside the climatic chamber.

Figure 26(b) shows the variation of λ_B for different temperatures and humidity. When comparing the wavelength shift with Figure 26(a), it is observed that temperature is a more influential factor in $\Delta\lambda_B$. While the maximum $\Delta\lambda_B$ in the submersion test was close to 0.15 nm, in the test conducted in the climatic chamber, $\Delta\lambda_B$ varies by 0.2 nm for a ΔT of 5 °C. This difference in sensitivity between the tests is expected because the sensitivity of FBG is directly associated with strain and temperature variations. Therefore, the multifunctional structure being used has a greater capacity for heat exchange between the external environment and the FBG sensor, rather than causing deformation due to variations in humidity.

Another aspect of Figure 26(b) is that the sensitivity of FBG is affected by 40 °C, and the value of $\Delta\lambda_B$ is expected to continue to increase along with temperature. In the temperature range of 25 °C to 40 °C, the sensor showed a high linearity with R^2 above 0.98 and the average sensitivity calculated between the different curves of relative humidity was 33.02 pm /°C. This behavior shows that the expansion of the optical fiber is related to the expansion of the structure, which saturated the periodic modulation of the FBG.

4.4 Accelerometer cantilever

Figure 27 shows the fabricated accelerometer cantilevers. Figure 27(a) shows the structure manufactured with 17-4 PH and M represents the inertial mass of the manufactured structure. The variation of this mass results in a variation in the cantilever strain, which also varies the deformation in the FBG. Furthermore, it is shown how the optical fiber is positioned within the structure, indicating the positioning of the FBG. Figure 27(b) shows the structures manufactured with the nylon filament fixed to a base printed with nylon filament. This base is adapted for fixing the cantilevers in the vibration generator for both cantilevers' characterization. The natural frequencies of the cantilevers were calculated using Equation 2.6 and are shown in Table 3. For the calculation, it was necessary to take measurements from the accelerometers and estimate the

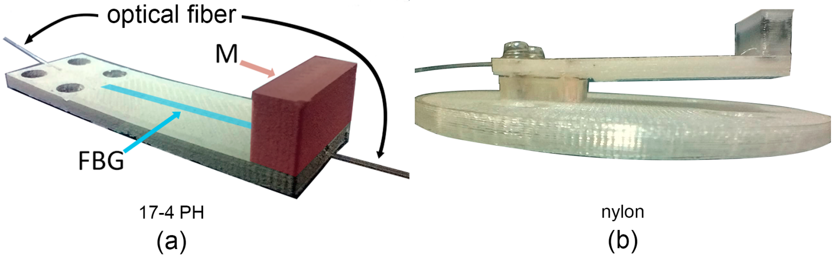

Figure 27 – Accelerometer cantilevers embedded with FBG.

density of the materials after printing, as well as obtain the *E* of both materials from the dynamic mechanical tests at 25 °C temperature. The tip mass value of each accelerometer varies according to the density of the material since the same model was used to print both accelerometers. As nylon is a light material compared to the 17-4 PH filament, a standard mass of 10 g was added to the tip of the accelerometer to reduce its natural frequency.

	L (mm)	**b (mm)**	**h (mm)**	ρ **(kg/m^3)**	**M (g)**	m_{bean} **(g)**	**E (MPa)**	$\omega_n/2\pi$ **(Hz)**
17-4 PH	29.0	12.95	2.00	4789.5	1.2	3.60	282.6	60.3
Nylon	29.0	13.30	2.75	1069.4	10.3	1.13	141.9	31.1

Table 3 – Construction information and physical properties of manufactured accelerometers.

Figure 28 shows the result of the signal collected from the 17-4 PH and nylon cantilevers after passing through the FFT. This figure shows the cantilever signal when subjected to the generated with an amplitude of 0.5 V. It is evident from the figures that the amplitude peaks do not precisely align with the frequency at which the vibration generator is set. This discrepancy is easily noticeable in the 17-4 PH cantilever at both 10 Hz and 100 Hz frequencies. The deviation observed in the 17-4 PH readings can be interpreted as a systematic deviation occurring between the input and output of the sinusoidal signal. Additionally, the nylon cantilever exhibits a peak nearly double that of the applied vibration frequency by the shaker, mainly at 10 Hz. This suggests the presence of some mechanical looseness in the nylon accelerometer when it was fixed on the shaker structure during the test. Furthermore, when subjected to a frequency of 100 Hz, the sensor signal presents a noisy response in the FFT analysis, with no amplitude peaks within the spectrum resulting from the analysis. This noise introduces fluctuations that directly impact the sensitivity results.

Figure 29 shows the sensitivity of the structures with respect to the variation in the amplitude of the vibration generated. For the 17-4 PH cantilever, the sensitivity was calculated using linear regressions, and for the different frequencies at which the cantilever was subjected, it presented different sensitivities. This occurs because the acceleration is greater for higher vibration frequencies, just as the variation in the FBG wavelength will have a greater modulus and is also enhanced by the increase in amplitude. With the regression, the amplitude values are represented as 98.15% and 97.03% for the frequencies of 10 Hz and 100 Hz, respectively.

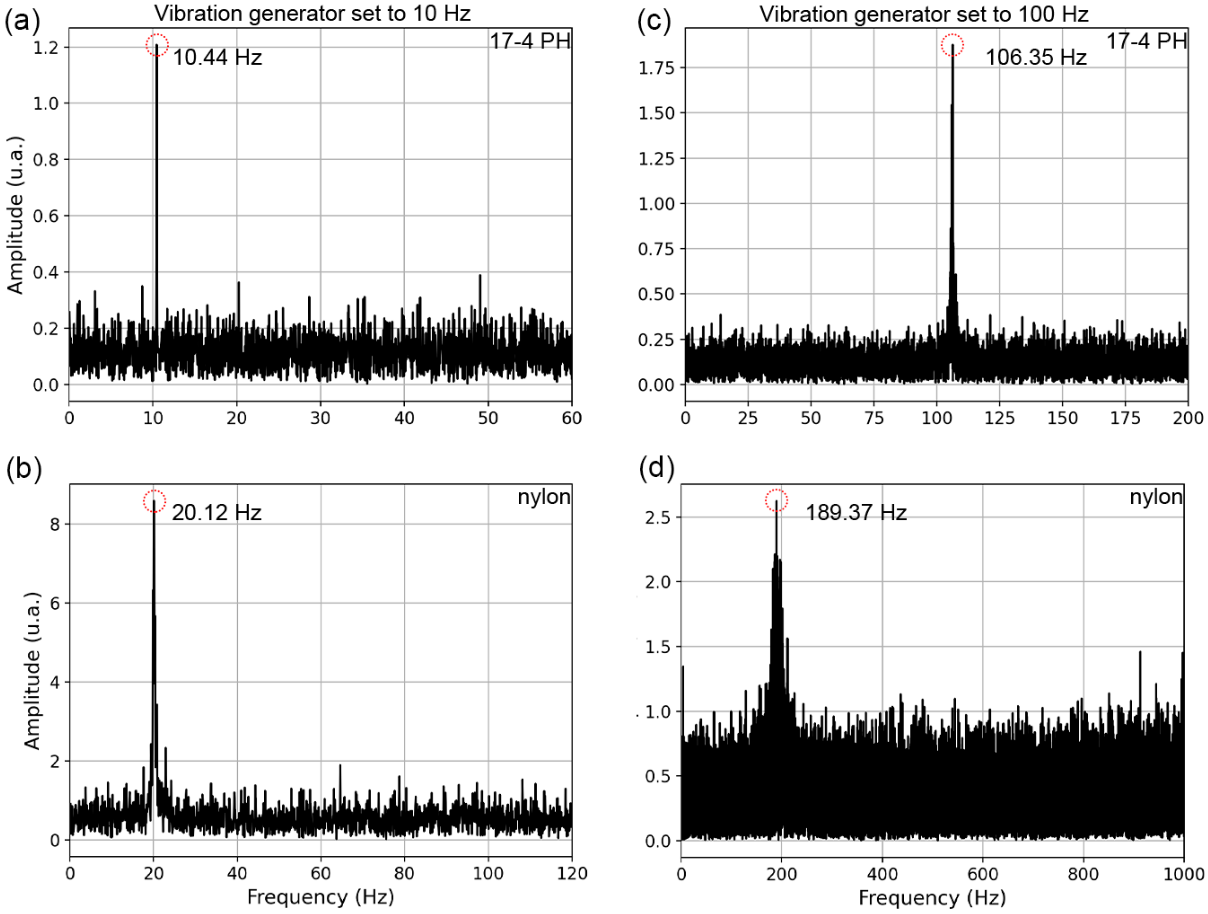

Figure 28 – Cantilever signal after FFT. The vibration generator was set to 10 Hz in (a) and (b), and to 100 Hz in (c) and (d), with an amplitude of 0.5 V.

Furthermore, the calculated sensitivity for these frequencies was 1.79 pm/V and 3.61 pm/V, with the 17-4 PH cantilever being more sensitive at higher frequency. A second-degree polynomial regression was required for the nylon cantilever due to the multiple vibration modes. However, even with this regression, only 94.10% of the cantilever's vibration pattern could be accurately represented. From the data of the vibration amplitude, it is possible to infer the wavelength shift amplitude with a root mean squared error of around 8.046 pm. It was not feasible to calculate the sensitivity of this cantilever when subjected to 100 Hz. This was due to the significant amount of noise in the measurements, which made it impossible to accurately determine the wavelength variation's amplitude.

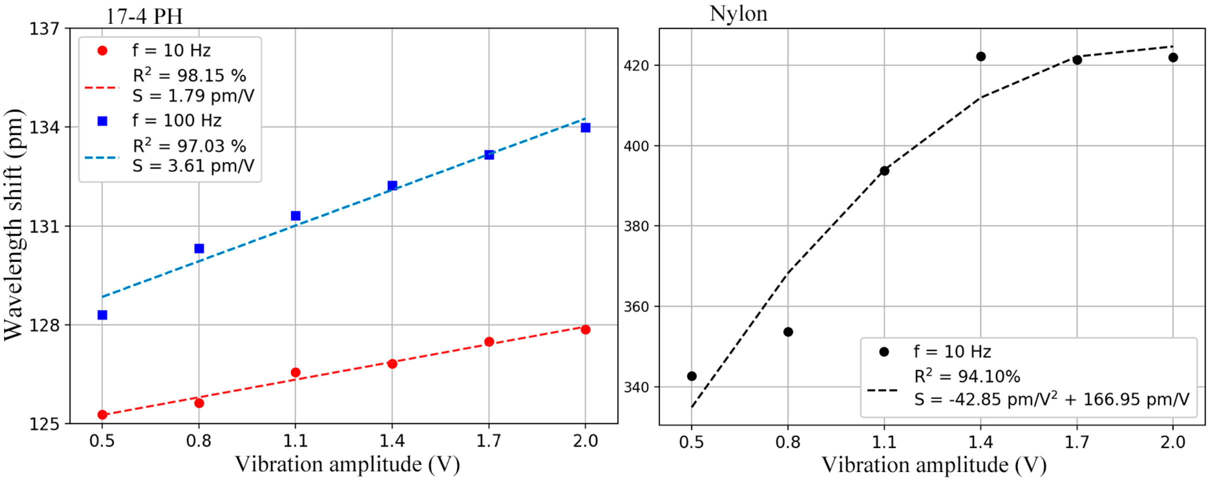

Figure 29 – Cantilevers sensitivities calculated due to the imposed vibration amplitude.

5 Final Remarks and Future Works

This Master's Dissertation presents the development of multifunctional structures fabricated through additive manufacturing and embedded with optical fiber sensors. The fabrication process of these structures encompassed various techniques. The structure designed for temperature measurement across diverse environments was constructed using light-cured resin. The flexible artificial tendon, on the other hand, was created through Fused Filament Fabrication (FFF), where molds were produced to shape the tendon, followed by the flow of polyurethane (PU) resin (thermopolymerizable) into these molds to achieve the desired tendon shape. In addition, the frequency acquisition cantilevers were directly manufactured using FFF, employing filaments with distinct mechanical properties.

In the materials characterizations, it was observed that increasing the cross section of a manufactured body, either by increasing the filling or augmenting the wall thickness, also enhances the mechanical resistance of the body, as represented by Young's modulus. However, despite its micrometric dimensions, optical fiber exerts a significant influence on these flexible materials. This implies that manufacturing parameters are not as influential on the modulus of a body as the amount of embedded fiber. Regarding dynamic characterizations, the influence of the amorphous chains of the nylon polymer is observed on its modulus at the glass transition temperature and above the plateau. In contrast, the 17-4 PH compound does not exhibit a discrepancy in its modulus for the imposed frequencies.

The artificial tendon structure was characterized by the parameters of strain, temperature, and angle. For strain, FBGs within the tendon presented different sensitivities, the sensitivity of FBG2 and FBG3 (which were closer to the walls) was calculated at 0.237 pm/$\mu\varepsilon$ and 0.242 pm/$\mu\varepsilon$, respectively, while FBG1 (which was in the center of the tendon) was 0.647 pm/$\mu\varepsilon$. In the temperature test, the FBGs had similar sensitivity, with the average between them being 9.06 pm/°C. The tendon was also subjected to angle characterization, which could be estimated through a polynomial relationship with the optical power reflected by the FBGs and the wavelength shift presenting a root mean squared error of around 3.25 °.

The temperature sensor designed demonstrated a range limitation compared to temperature sensors already produced with FBG. Consequently, it will be necessary to implement a new methodology for the manufacture of this type of structure. The 17-4 PH cantilever presented a linear relation to the vibration amplitude, with a sensitivity of 1.79 pm/V and 3.61 pm/V for 10 Hz and 100 Hz vibration frequencies, respectively. For the nylon cantilever, a polynomial regression was applied and a root mean squared error of around 8.046 pm was calculated.

In future work, the multifunctional structures produced in this work have the potential to be applied to segments that require sensors to measure strain, temperature, curvature angle, and vibration frequency. The artificial tendon can be part of cable actuators in exoskeletons or orthoses, so that when assembled with the steel cable it is capable of measuring the tension or force used during actuation. With the tendon, it is also possible to measure the curvature angle, which can be applied to measure the reach of a patient undergoing knee rehabilitation, for example. The cantilever can be characterized at different frequencies and applied in vibration monitoring systems to prevent failures, as it can be applied without impacting the system dynamics as it is light and compact. These characteristics are favorable for the implementation of multifunctional structures, in addition to their measurement capacity.

References

[1] A. Lendlein e R. S. Trask, “Multifunctional materials: concepts, function-structure relationships, knowledge-based design, translational materials research,” *Multifunctional Materials*, v. 1, n. 1, p. 010 201, 2018.

[2] M. Silverio-Fernández, S. Renukappa e S. Suresh, “What is a smart device?-a conceptualisation within the paradigm of the internet of things,” *Visualization in Engineering*, v. 6, n. 1, pp. 1–10, 2018.

[3] S. Lee, Q. Shi e C. Lee, “From flexible electronics technology in the era of IoT and artificial intelligence toward future implanted body sensor networks,” *APL Materials*, v. 7, n. 3, 2019.

[4] H. Gu, Y. Moslehy, D. Sanders, G. Song e Y. Mo, “Multi-functional smart aggregate-based structural health monitoring of circular reinforced concrete columns subjected to seismic excitations,” *Smart Materials and Structures*, v. 19, n. 6, p. 065 026, 2010.

[5] M. Xie, K. Hisano, M. Zhu et al., “Flexible multifunctional sensors for wearable and robotic applications,” *Advanced Materials Technologies*, v. 4, n. 3, p. 1 800 626, 2019.

[6] C. L. Roozeboom, B. E. Hill, V. A. Hong et al., “Multifunctional integrated sensors for multiparameter monitoring applications,” *Journal of Microelectromechanical Systems*, v. 24, n. 4, pp. 810–821, 2014.

[7] S. C. Farina, E. Kane e L. P. Hernandez, “Multifunctional structures and multistructural functions: integration in the evolution of biomechanical systems,” *Integrative and Comparative Biology*, v. 59, n. 2, pp. 338–345, 2019.

[8] Y. Xiong e F. Xu, “Multifunctional integration on optical fiber tips: challenges and opportunities,” *Advanced Photonics*, v. 2, n. 6, pp. 064 001–064 001, 2020.

[9] A. Leal-Junior, L. Avellar, V. Biazi, M. S. Soares, A. Frizera e C. Marques, “Multifunctional flexible optical waveguide sensor: On the bioinspiration for ultrasensitive sensors development,” *Opto-Electronic Advances*, v. 5, n. 10, pp. 210 098–1, 2022.

[10] T. J. Koob, “Biomimetic approaches to tendon repair,” *Comparative Biochemistry and Physiology Part A: Molecular & Integrative Physiology*, v. 133, n. 4, pp. 1171–1192, 2002.

[11] G. d. P. Rubio, F. M. R. Martins Ferreira, F. H. d. L. Brandão et al., “Evaluation of commercial ropes applied as artificial tendons in robotic rehabilitation orthoses,” *Applied Sciences*, v. 10, n. 3, p. 920, 2020.

[12] R. C. Silva, B. G. Lourenço, P. H. Ulhoa et al., “Biomimetic design of a tendon-driven myoelectric soft hand exoskeleton for upper-limb rehabilitation,” *Biomimetics*, v. 8, n. 3, p. 317, 2023.

[13] L. Wang, Z. Lou, K. Jiang e G. Shen, “Bio-multifunctional smart wearable sensors for medical devices,” *Advanced Intelligent Systems*, v. 1, n. 5, p. 1 900 040, 2019.

[14] T. Li, Y. Li e T. Zhang, “Materials, structures, and functions for flexible and stretchable biomimetic sensors,” *Accounts of chemical research*, v. 52, n. 2, pp. 288–296, 2019.

[15] S. Malwade, S. S. Abdul, M. Uddin et al., “Mobile and wearable technologies in healthcare for the ageing population,” *Computer methods and programs in biomedicine*, v. 161, pp. 233–237, 2018.

[16] C. Marques, A. Leal-Júnior e S. Kumar, “Multifunctional integration of optical fibers and nanomaterials for aircraft systems,” *Materials*, v. 16, n. 4, p. 1433, 2023.

[17] A. G. Leal-Junior, A. Frizera, L. Vargas-Valencia et al., “Polymer optical fiber sensors in wearable devices: Toward novel instrumentation approaches for gait assistance devices,” *IEEE sensors journal*, v. 18, n. 17, pp. 7085–7092, 2018.

[18] C. A. Diaz, A. Leal-Junior, C. Marques et al., “Optical fiber sensing for sub-millimeter liquid-level monitoring: A review,” *IEEE sensors journal*, v. 19, n. 17, pp. 7179–7191, 2019.

[19] A. G. Leal-Junior, V. Campos, C. Díaz, R. M. Andrade, A. Frizera e C. Marques, “A machine learning approach for simultaneous measurement of magnetic field position and intensity with fiber Bragg grating and magnetorheological fluid,” *Optical Fiber Technology*, v. 56, p. 102 184, 2020.

[20] A. Leal-Junior, L. Avellar, A. Frizera e C. Marques, “Smart textiles for multimodal wearable sensing using highly stretchable multiplexed optical fiber system,” *Scientific Reports*, v. 10, n. 1, p. 13 867, 2020.

[21] E. Udd, “The emergence of fiber optic sensor technology,” *Fiber Optic Sensors: An Introduction for Engineers and Scientists*, pp. 1–8, 2011.

[22] A. G. Leal-Junior, C. A. Diaz, L. M. Avellar, M. J. Pontes, C. Marques e A. Frizera, “Polymer optical fiber sensors in healthcare applications: A comprehensive review,” *Sensors*, v. 19, n. 14, p. 3156, 2019.

[23] M. Jurak, A. E. Wiącek, A. Ładniak, K. Przykaza e K. Szafran, “What affects the biocompatibility of polymers?” *Advances in Colloid and Interface Science*, v. 294, p. 102 451, 2021.

[24] A. Awasthi, K. K. Saxena e R. K. Dwivedi, “An investigation on classification and characterization of bio materials and additive manufacturing techniques for bioimplants,” *Materials Today: Proceedings*, v. 44, pp. 2061–2068, 2021.

[25] Y. Wu, Y. Lu, M. Zhao, S. Bosiakov e L. Li, “A critical review of additive manufacturing techniques and associated biomaterials used in bone tissue engineering,” *Polymers*, v. 14, n. 10, p. 2117, 2022.

[26] R. Ilyas, S. Sapuan, M. Harussani et al., “Polylactic acid (PLA) biocomposite: Processing, additive manufacturing and advanced applications,” *Polymers*, v. 13, n. 8, p. 1326, 2021.

[27] M. Griffin, N. Castro, O. Bas, S. Saifzadeh, P. Butler e D. W. Hutmacher, “The current versatility of polyurethane three-dimensional printing for biomedical applications,” *Tissue Engineering Part B: Reviews*, v. 26, n. 3, pp. 272–283, 2020.

[28] J. Yin, J. Zhong, J. Wang et al., “3D-printed high-density polyethylene scaffolds with bioactive and antibacterial layer-by-layer modification for auricle reconstruction,” *Materials Today Bio*, v. 16, p. 100 361, 2022.

[29] E. H. Backes, S. V. Harb, C. A. G. Beatrice et al., “Polycaprolactone usage in additive manufacturing strategies for tissue engineering applications: A review,” *Journal of Biomedical Materials Research Part B: Applied Biomaterials*, v. 110, n. 6, pp. 1479–1503, 2022.

[30] J. K. Placone e A. J. Engler, “Recent advances in extrusion-based 3D printing for biomedical applications,” *Advanced healthcare materials*, v. 7, n. 8, p. 1 701 161, 2018.

[31] I. Gibson, D. W. Rosen, B. Stucker et al., *Additive manufacturing technologies*. Springer, 2021, vol. 17.

[32] J. Pierre, F. Iervolino, R. D. Farahani, N. Piccirelli, M. Lévesque e D. Therriault, “Material extrusion additive manufacturing of multifunctional sandwich panels with load-bearing and acoustic capabilities for aerospace applications,” *Additive Manufacturing*, v. 61, p. 103 344, 2023.

[33] M. Majumder, T. K. Gangopadhyay, A. K. Chakraborty, K. Dasgupta e D. K. Bhattacharya, “Fibre Bragg gratings in structural health monitoring—Present status and applications,” *Sensors and Actuators A: Physical*, v. 147, n. 1, pp. 150–164, 2008.

[34] D. Lo Presti, A. Carnevale, J. D’Abbraccio et al., “A multi-parametric wearable system to monitor neck movements and respiratory frequency of computer workers,” *Sensors*, v. 20, n. 2, p. 536, 2020.

[35] Z. Fang, K. Chin, R. Qu e H. Cai, *Fundamentals of optical fiber sensors*. John Wiley & Sons, 2012, vol. 226.

[36] G. Rajan, *Optical fiber sensors: advanced techniques and applications*. CRC press, 2017.

[37] A. G. Leal-Junior, C. A. Díaz, A. Frizera, C. Marques, M. R. Ribeiro e M. J. Pontes, “Simultaneous measurement of pressure and temperature with a single FBG embedded in a polymer diaphragm,” *Optics & Laser Technology*, v. 112, pp. 77–84, 2019.

[38] D. Barrera, C. Silvestre, M. Cruz et al., “Development of a Multi-point Multi-parametric Sensor for Structural Health Monitoring,” em *2007 International Conference on Sensor Technologies and Applications (SENSORCOMM 2007)*, IEEE, 2007, pp. 46–51.

[39] V. Biazi-Neto, C. A. Marques, A. Frizera-Neto e A. G. Leal-Junior, "FBG-embedded robotic manipulator tool for structural integrity monitoring from critical strain-stress pair estimation," *IEEE Sensors Journal*, v. 22, n. 6, pp. 5695–5702, 2022.

[40] A. G. Leal-Junior, W. Coimbra, C. Marques e A. Frizera, "Highly stretchable polymer optical fiber for mechanical sensing in artificial tendons: Towards novel sensors for soft robotics," em *Actuators*, MDPI, vol. 9, 2020, p. 125.

[41] Y.-x. Guo, D.-s. Zhang, Z.-d. Zhou, F.-d. Zhu, L. Xiong e T.-l. Li, "Cantilever based FBG vibration transducer with sensitization structure," *Optoelectronics Letters*, v. 9, n. 6, pp. 410–413, 2013.

[42] L. Hong, R. Sun, Z. Qiu, Z. Han e Y. Li, "A multi-cantilever beam low-frequency FBG acceleration sensor," *Scientific Reports*, v. 11, n. 1, p. 18 502, 2021.

[43] P. Stavropoulos, *Additive Manufacturing: Design, Processes and Applications*. Springer Nature, 2023.

[44] E. Pei, I. R. Kabir e B. Leutenecker-Twelsiek, "History of AM," em *Springer Handbook of Additive Manufacturing*, Springer, 2023, pp. 3–29.

[45] S. ISO, "ASTM 52900: 2017," *Standard Terminology for Additive Manufacturing–General Principles–Terminology*, v. 24, 2017.

[46] K. Zhou, *Additive Manufacturing: Materials, Functionalities and Applications*. Springer Nature, 2022.

[47] V. V. Popov, M. L. Grilli, A. Koptyug et al., "Powder Bed Fusion Additive Manufacturing Using Critical Raw Materials: A Review," *Materials*, v. 14, n. 4, 2021, ISSN: 1996-1944. DOI: `10.3390/ma14040909`. endereço: `https://www.mdpi.com/1996-1944/14/4/909`.

[48] S. Wolff, "Directed Energy Deposition," em *Springer Handbook of Additive Manufacturing*, Springer, 2023, pp. 459–474.

[49] A. Haghighi, "Material Extrusion," em *Springer Handbook of Additive Manufacturing*, Springer, 2023, pp. 335–347.

[50] G. Gao, B. S. Kim, J. Jang e D.-W. Cho, "Recent strategies in extrusion-based three-dimensional cell printing toward organ biofabrication," *ACS Biomaterials Science & Engineering*, v. 5, n. 3, pp. 1150–1169, 2019.

[51] P. Jiang, Z. Ji, X. Zhang, Z. Liu e X. Wang, "Recent advances in direct ink writing of electronic components and functional devices," *Progress in Additive Manufacturing*, v. 3, pp. 65–86, 2018.

[52] A. Paolini, S. Kollmannsberger e E. Rank, "Additive manufacturing in construction: A review on processes, applications, and digital planning methods," *Additive manufacturing*, v. 30, p. 100 894, 2019.

[53] M. R. Hassan, H. W. Jeon, G. Kim e K. Park, “The effects of infill patterns and infill percentages on energy consumption in fused filament fabrication using CFR-PEEK,” *Rapid Prototyping Journal*, v. 27, n. 10, pp. 1886–1899, 2021.

[54] A. Méndez e T. F. Morse, *Specialty optical fibers handbook*. Elsevier, 2011.

[55] C. Yeh, *Handbook of fiber optics: Theory and applications*. Academic Press, 2013.

[56] T. R. Woliński, “I Polarimetric optical fibers and sensors,” em *Progress in Optics*, vol. 40, Elsevier, 2000, pp. 1–75.

[57] R. Kashyap, *Fiber bragg gratings*. Academic press, 2009.

[58] S. James, M. Dockney e R. Tatam, “Simultaneous independent temperature and strain measurement using in-fibre Bragg grating sensors,” *Electronics Letters*, v. 32, n. 12, pp. 1133–1134, 1996.

[59] S. R. Baker, H. N. Rourke, V. Baker e D. Goodchild, “Thermal decay of fiber Bragg gratings written in boron and germanium codoped silica fiber,” *Journal of Lightwave Technology*, v. 15, n. 8, pp. 1470–1477, 1997.

[60] S. C. Warren-Smith, E. P. Schartner, L. V. Nguyen et al., “Stability of grating-based optical fiber sensors at high temperature,” *IEEE Sensors Journal*, v. 19, n. 8, pp. 2978–2983, 2019.

[61] D. J. Inman e R. C. Singh, *Engineering vibration*. Prentice Hall Englewood Cliffs, NJ, 1994, vol. 3.

[62] D. ASTM, “ASTM D-638,” *Standard test method for tensile properties of plastics. ASTM Int*, 2014.

[63] K. P. Menard e N. Menard, *Dynamic mechanical analysis*. CRC press, 2020.

[64] J. C. Mankins et al., “Technology readiness levels,” *White Paper, April*, v. 6, n. 1995, p. 1995, 1995.

APPENDIX A – Additional Information

A.1 Technology Readiness Level (TRL) Scale

TRL	Definition	Description
1	Basic principles observed and reported.	The lowest "level" of technology maturation. At this level, scientific research begins to be translated into applied research and development.
2	Technology concept and/or application formulated.	Once basic physical principles are observed, then at the next level of maturation, practical applications of those characteristics can be 'invented' or identified. At this level, the application is still speculative: there is not experimental proof or detailed analysis to support the conjecture.
3	Analytical and experimental critical function and/or characteristic proof of concept.	At this step in the maturation process, active research and development (R&D) is initiated. This must include both analytical studies to set the technology into an appropriate context and laboratory-based studies to physically validate that the analytical predictions are correct. These studies and experiments should constitute proof of concept validation of the applications/concepts formulated at TRL 2.
4	Component and/or breadboard validation in laboratory environment.	Following successful proof of concept work, basic technological elements must be integrated to establish that the "pieces" will work together to achieve concept-enabling levels of performance for a component and/or breadboard. This validation must devised to support the concept that was formulated earlier, and should also be consistent with the requirements of potential system applications. The validation is relatively "low-fidelity" compared to the eventual system: it could be composed of ad hoc discrete components in a laboratory.
5	Component and/or breadboard validation in relevant environment.	At this, the fidelity of the component and/or breadboard being tested has to increase significantly. The basic technological elements must be integrated with reasonably realistic supporting elements so that the total applications (component-level, sub-system-level, or system-level) can be tested in a simulated or somewhat realistic environment. From one-to-several new technologies might be involved in the demonstration.

Adapted from [64].

TRL	Definition	Description
6	System/subsystem model or prototype demonstration in a relevant environment.	A major step in the level of fidelity of the technology demonstration follows the completion of TRL 5. At TRL 6, a representative model or prototype system or system would be tested in a relevant environment. Of course, the demonstration should be successful to represent a true TRL 6. Not all technologies will undergo a TRL 6 demonstration: at this point, the maturation step is driven more by assuring management confidence than by R&D requirements. The demonstration might represent an actual system application, or it might only be similar to the planned application, but using the same technologies. At this level, several to many new technologies might be integrated into the demonstration.
7	System prototype demonstration in an operational environment.	The prototype should be near or at the scale of the planned operational system. The driving purposes for achieving this level of maturity are to assure system engineering and development management confidence (more than for purposes of technology R&D). Therefore, the demonstration must be of a prototype of that application.
8	Actual system completed and qualified through test and demonstration.	All technologies being applied in actual systems go through TRL 8. In almost all cases, this level represents the end of true system development.
9	Actual system has proven through successful operations.	All technologies being applied in actual systems go through TRL 9. In almost all cases, the end of the last ‘bug fixing’ aspects of true ‘system development’.This might include integration of new technology into an existing system.

Adapted from [64].